J. Appl. Comput. Mech., xx(x) (2026) 1-19
DOI: 10.22055/jacm.2026.48911.5593

ISSN: 2383-4536
jacm.scu.ac.ir

Shahid Chamran University of Ahvaz

Journal of Applied and Computational Mechanics

Research Paper

Numerical Study on Energy Loss and Gas-Liquid Two-Phase Mixing Characteristics in Overflow Carbonizer Reactor with Integrated Venturi-Porous Media Structure

Yejie Gu[1], Hongyu Pan[1], Yijie Zhuang[1], Congcong Ren[2], Quanquan Luo[2]

[1] School of Environmental Science and Engineering, Guangdong University of Technology, Guangzhou, 510006, China
[2] Foshan Shunde Midea Water Dispenser Manufacturing Co., Ltd, Foshan, 528300, China

Received November 14 2025; Revised January 28 2026; Accepted for publication February 24 2026.
✉ Corresponding authors: Y. Zhuang (zyj7933@gdut.edu.cn); Q. Luo (luoqq21@midea.com)

Abstract. This study proposes a gas-liquid reactor model integrating a venturi tube and porous media, aiming to enhance gas-liquid mixing efficiency by inducing turbulence and improve CO_2 dissolution and carbonation efficiency. Compared with conventional carbonizer devices, the proposed system effectively improves CO_2 dissolution and reaction efficiency by designing a novel venturi structure to induce turbulence and combining the advantages of porous media for enhanced mass transfer. This paper establishes a CO_2 bubble observation and concentration testing platform, and uses CFD methods to simulate the fluid dynamics characteristics and CO_2 concentration distribution under different operating conditions and porous medium structural parameters. Special attention is paid to the effects of gas-liquid inlet flow rates, porous media filling configurations, and pore structure properties on pressure loss, carbonation efficiency, and energy consumption. The results demonstrate that the gas-liquid inlet flow rates of 7 and 1.8 L/min achieve optimal carbonation concentration (8-10 g/L) with balanced energy consumption. Partial filling of porous media in a 1-3 configuration reduces pressure drop by 5% while enhancing H_2CO_3 formation by 5%. A porosity of 0.8 and pore size of 15-20 PPI maximize CO_2 dissolution (8.2 g/L) with minimal operational pressure (< 0.874 MPa). The system proves that within 1.6 s, the usage of porous media placement significantly affects transient pressure spikes and concentration uniformity. The present study may not only provide novel insights for the optimization and design of gas-liquid reactors, but also offer feasible solutions for carbon capture and storage technology.

Keywords: Gas-liquid reactor; Porous media; Mass transfer; Energy loss; CO_2 dissolution.

1. Introduction

As global warming concerns mount, CO_2 emission reduction, especially CO_2 capture technology, has gained increasing attention [1]. CO_2-water interaction underpins CCS (carbon capture and storage), EOR (enhanced oil recovery), and carbonated drink production [2-4]. Enhancing CO_2 solubility in aqueous media is critical for environmental engineering, energy storage systems, and industrial applications spanning chemical processing and food manufacturing [5, 6]. A gas-liquid reactor integrates mass transfer across the gas-liquid interface with chemical reactions, dispersing CO_2 into micro-bubbles or liquid films to ensure thorough contact with water [7]. It utilizes techniques like injection, agitation, and flow guiding to enhance mass transfer, acting as the key apparatus for boosting CO_2 dissolution and reaction in water-based systems [8]. Over the past few decades, process intensification reactors such as venturi tubes [9, 10], membrane reactors [11, 12], bubble column reactors [13, 14], and porous media packed tanks [15, 16] have been continuously developed and optimized. However, traditional gas-liquid reactors are still constrained by issues such as low mass transfer efficiency, limited reaction kinetics, and poor operational stability, which hinder the industrialization and large-scale development of the CO_2-water reaction process. Therefore, developing efficient and stable gas-liquid reactors and exploring reaction enhancement mechanisms are of great theoretical significance and practical value for promoting low-carbon technological innovation and sustainable development.

In the design and optimization of gas-liquid reactors, scholars have conducted extensive research using experimental methods. Early experimental studies focused primarily on the basic operating performance of gas-liquid reactors, such as the effects of bubble size [17], gas flow rate [18], and liquid flow rate on reactor performance [19]. With the continuous advancement of experimental techniques, researchers can now use particle image velocimetry (PIV) and high-speed cameras to observe dynamic processes at gas-liquid interfaces in detail, thereby obtaining the motion characteristics and evolution patterns of bubble groups [20]. Zhai et al. [21] used structured plane laser-induced fluorescence and PIV to measure the true gas-liquid interface and velocity distribution in two-phase flow. Based on the evolution of the gas-liquid interface morphology, three plug flow aeration mechanisms were identified: shear stress mechanism, leading vortex mechanism, and gas entrainment mechanism. Ouyang et al. and Chen et al. [22, 23]

Published online: February 25 2026

conducted a systematic study on the two-phase flow evolution in a gas-liquid vortex reactor (GLVR) using high-speed imaging and digital image analysis. The results showed that gas bubbles and liquid ligaments were observed across a wide operating window. Bi et al. [24] used particle image velocimetry (PIV) and CCD cameras combined with image processing technology to acquire reliable bubble size images in a gas-liquid loop reactor. They conducted a detailed study on the effects of gas phase velocity, liquid phase velocity, draft tube diameter, and nozzle installation position on bubble size distribution. Although experimental methods can provide important insights into the operational behavior of gas-liquid reactors, they still have significant limitations in spatial resolution, visualization capabilities, and quantitative analysis of complex flow and mass transfer phenomena. Furthermore, large-scale experiments are often time-consuming, labor-intensive, and costly, making it difficult to cover all operating conditions.

In recent years, high-precision numerical simulation of gas-liquid flow and mass transfer processes based on computational fluid dynamics (CFD) methods has become an important means to complement experimental research and reveal the internal flow mechanisms of gas-liquid reactors [25, 26]. Kumari et al. [27] performed numerical simulations of stirred reactors using the Euler-Euler two-fluid model and the standard k-ε turbulence model. They experimentally verified the simulation results using a high-speed camera and found that the simulation results showed good consistency with the experimental photographs. Jie et al. [8] used the Eulerian two-fluid model to study the gas-liquid mass transfer enhancement effect of ethanolamine-iron (MEA-Fe) solution in a cavitation jet reactor with radial spiral holes. They revealed that the radial spiral holes enhanced fluid turbulence to increase the reactant contact area, thereby improving gas-liquid mass transfer efficiency. Teli and Mathpati [28] employed the Eulerian two-fluid model along with experimental measurements to systematically analyze the gas/liquid holdup, liquid circulation velocity, and axial velocity distribution in an external-loop gas reactor under low-flow conditions. They also evaluated the applicability of different mass-transfer models and validated the selected models. Numerous studies have demonstrated that the transient flow characteristics predicted by the CFD Euler-Euler method can accurately represent actual gas-liquid mass transfer phenomena, and these predictions show close agreement with experimental results [29-31].

As a classic gas-liquid reactor, the venturi tube is widely used in the study of gas-liquid mixing, mass transfer, and chemical reaction processes due to its unique fluid dynamic characteristics [32]. Its working principle is based on the venturi effect. When fluid flows through a venturi tube, the flow velocity increases significantly as it passes through the narrow section of the throat, while the corresponding pressure decreases. This pressure difference and the resulting high-speed flow increase the contact area between the gas and liquid phases, which is conducive to gas-liquid mass transfer and reaction processes [33]. A conventional venturi bubble generator includes an inlet, a contraction section, a throat section, a divergent section, and an outlet [34]. Liu et al. [35] discussed the effects of these five structural parameters on gas content and energy loss, and determined the optimal structure of the venturi tube. Zhou et al. [36] combined PIV experiments with CFD simulations to propose a novel double-inlet venturi injector reactor structure and investigated the relationship between its structure and performance. Chen et al. [37] studied the gas-liquid flow field, bubble behavior, and mass transfer capacity in the divergent section and compared the mass transfer efficiency of single-inlet tube venturi devices and double-inlet tube venturi devices. However, the previous venturi inlet was located in a narrow throat passage, which structurally limited the efficiency of gas-liquid mixing [38], requiring the venturi tube structure to be redesigned and optimized.

Porous media, characterized by their high specific surface area, complex flow channel architecture, and strong flow disturbance capability, are widely applied in various reaction systems, including gas absorption [39, 40], heat transfer enhancement [41, 42], and wastewater treatment [43, 44]. To further improve mass transfer efficiency and reaction performance in gas-liquid reactors, an increasing number of researchers are focusing on packing reactors with porous media to enhance gas-liquid phase contact and mixing. Tang et al. [45] designed a bubble tower filled with porous media for treating three-phase systems of gas reactants with strong exothermic reactions. The study found that gas holding capacity increased as the packing size decreased, and that liquid circulation velocity decreased as the packing particle size decreased due to increased flow resistance. Li et al. [46] used an experimental system integrating PIV and high-speed camera techniques to study the effects of liquid velocity and viscosity on vortex formation in porous matrix. The results showed that porous media facilitate the formation of small vortex structures at the gas-liquid interface, thereby enhancing the gas-liquid mass transfer process. Mao et al. [47] designed a rotating foam agitator incorporating porous media to enhance mass transfer in multiphase systems. The results indicated that bubble rupture in porous media was primarily driven by gas-solid interactions and liquid turbulent shear, thereby leading to enhanced mass transfer. Goel et al. [48] studied the hydrodynamics and CO_2 capture process using porous solid adsorbents in a fluidized bed. They found that the particle bed exhibited intermittent flow behavior at different stages of fluidization transition, and that the CO_2 breakthrough curve was most sensitive to the mass transfer coefficient. Studies on porous media have shown that the rational application of porous media to fill reactors can significantly improve gas-liquid contact efficiency, thereby enhancing mass transfer performance.

In summary, the Venturi tube gas-liquid reactor and porous media filling technique, with their unique fluid dynamics control capabilities and excellent gas-liquid interface enhancement effects, have gradually become effective measures for improving gas-liquid reaction efficiency and enhancing mass transfer performance. However, the gas-liquid mixing efficiency of traditional Venturi tubes remains relatively low, and most studies on porous media filling have focused on improving macro-level performance, while the correlation between porous media microstructural parameters and mass transfer behavior has not been thoroughly explored. Therefore, this study proposes a gas-liquid reactor model that integrates a venturi tube and porous media, primarily designed for the manufacturing of household sparkling water makers. And establishes a CO_2 bubble observation and concentration testing platform using a high-speed camera. CFD simulations are employed to investigate the fluid dynamics characteristics and CO_2 concentration distribution under various operating conditions and porous media structural parameters. The study focused on the effects of gas-liquid inlet flow rates, porous media filling configuration, and pore structure characteristics on pressure loss, carbonizer efficiency, and energy consumption. The research findings not only provide new insights for the optimization and design of gas-liquid reactors but also offer feasible solutions for carbon capture and storage technology.

2. Mathematical Model

2.1. Problem description

Figure 1(a) shows the complete structure of the overflow carbonizer and the porous media filling scheme, a design primarily intended for the fabrication of household sparkling water makers. The overflow carbonizer features three main components: a venturi-type bubble generator, a porous medium filling tank and an outlet section. Figure 1(b) displays the specific dimensions of the overflow carbonizer. In the present study, the venturi used in the overflow carbonizer added an additional suction structure at the front end of the constriction section. This structure consists of three main parts: the inlet, the nozzle and the vacuum chamber. The novel design of the suction structure provides a larger driving space for the mixing and acceleration of the gas-liquid. After the cryogenic water and carbon dioxide gas enter from separate inlets, it is easier to develop fully in the vacuum chamber because of the faster flow rate at the gas inlet. And then due to the Venturi effect, the gas entering the throat channel segment mixes well with the fluid and produces an acceleration effect.

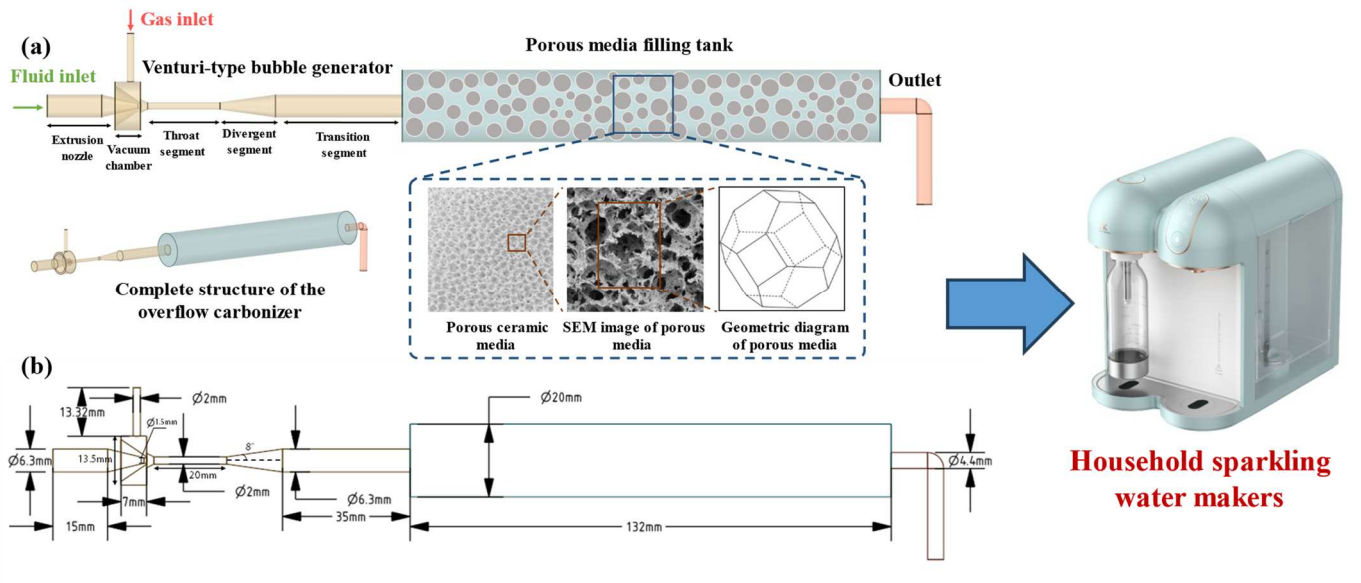

Fig. 1. (a) Overflow carbonizer complete structure and porous media filling scheme, (b) Specific dimensions of the overflow carbonizer.

This causes more gas to be entrained into the liquid stream, generating a pressure drop that promotes efficient gas-liquid mixing. The gas-liquid two phase fluid, which is fully mixed after the throat channel, induces turbulence to occur in the divergent segment, splitting the involved gas into more microbubbles.

The two-phase fluid flowing out of the Venturi tube bubble generator passes through the transition segment and flows into the porous media filling tank. Due to the high specific surface area of porous media, when two-phase fluids flow into porous media, they are split into numerous tiny bubbles, significantly increasing the gas-liquid contact area and thereby accelerating the carbonizer rate. Additionally, the pore structure of porous media suppresses large-scale vortices, inducing the fluid to generate microturbulence. The generation of microturbulence disrupts the mass transfer boundary layer, reduces mass transfer resistance, and enhances the absorption efficiency of CO_2. On the other hand, the resistance distribution of porous media is uniform, which can convert fluid pressure energy into kinetic energy, making the flow velocity more uniform across the cross section. This will prevent local liquid flooding or gas short circuiting.

Based on the above advantages of porous media, this paper adopts a porous media filling carbonization tank scheme to promote CO_2 absorption. In the selection of porous medium materials, ceramic porous media were chosen as the filling material for this study due to their chemical corrosion resistance, structural stability, and non-toxicity. The specific porous medium structure is shown in Fig. 1(a). Additionally, the relevant physical property parameters of the fluid water and carbon dioxide gas used in this study are given in Table 1.

It is worth noting that gas density affects gas-liquid mass transfer. Therefore, the density of CO_2 gas is determined by the ideal state equation below [31]:

$$\rho_g = \rho_{ref} \times \frac{P_{inlet}}{P_{ref}} \times \frac{T_{ref}}{T_{inlet}} \tag{1}$$

where, ρ_{ref}, P_{ref}, and T_{ref} represent the reference density, reference pressure, and reference temperature, respectively. In this paper, the values are: $\rho_{ref} = 1.8\ \mathrm{kg/m^3}$, $P_{ref} = 0.1\ \mathrm{Mpa}$, $T_{ref} = 298.15\ \mathrm{K}$.

2.2. Governing equations

2.2.1. *Eulerian two-fluid model*

The Euler-Euler method treats the two phases as mutually permeable continuous media, describing the motion of each phase from an Eulerian perspective. The Eulerian two-fluid method replaces the specific trajectories of fluid particles with volume-averaged phase fractions and velocities, providing bubble diameter and phase interface information based on coarse grids. In the Eulerian two-fluid method, the most commonly used models for considering gas-liquid two-phase flow involving bubbles are the VOF model and the Euler-Euler model. The VOF model requires a grid size smaller than the bubble or droplet size to accurately resolve the gas-liquid interface, consuming substantial computational resources and incurring high computational costs. The Euler–Euler model offers strong versatility, allowing the use of coarser mesh sizes while accounting for multiphase, multicomponent interfacial mass transfer. These advantages enable the model to consider interphase mass exchange and chemical reactions between components, making it suitable for studying CO_2 dissolution inside the overflow carbonizer [29].

Table 1. The physical property parameters of water and carbon dioxide gas.

Properties	Water	Carbon dioxide
Density (kg/m^3)	1000	See Eq. (1)
Specific heat capacity (J/kg·K)	4186	845
Thermal conductivity (W/m·K)	0.58	0.0165
Dynamic viscosity (Pa·s·10^{-3})	1.385	0.0140
Surface tension (N/m)	0.068	-
Diffusion coefficient (m^2/s·10^{-9})	-	1.46

Therefore, the Euler- Euler two-fluid model is used to simulate gas-liquid flow in an overflow carbonizer. In the Eulerian two-fluid model, the gas and liquid phases share the same pressure field, while the continuity equation and momentum equation for each phase are solved separately. The continuity equation and momentum equation can be expressed as [52]:

$$\nabla\cdot\left(\alpha_q\rho_q u_q\right)+\frac{\partial\left(\alpha_q\rho_q\right)}{\partial t}=\dot{m}_{gl} \tag{2}$$

$$\frac{\partial\left(\alpha_q\rho_q u_q\right)}{\partial t}+\nabla\cdot\left(\alpha_q\rho_q u_q u_q\right)=-\alpha_q\nabla P+\alpha_q\nabla\cdot\mu_{eff,q}\left(\nabla u_q+\nabla u_q^T\right)+F_{gl}+\alpha_q\rho_q\vec{g}+S_m+S_i \tag{3}$$

In the equation, the subscript l denotes the liquid phase, the subscript g denotes the gas phase, and the subscript q is the phase indicator symbol (which can refer to either the liquid phase or the gas phase). α, ρ, u represent the volume fraction, density, and velocity vector, respectively. And $\dot{m}_{gl}$ represents mass transfer between the gas and liquid phases. For cases without mass transfer, $\dot{m}_{gl}$ is equal to 0. The terms on the right-hand side of Eq. (2) are the pressure gradient force, stress-strain tensor, interphase interaction force, volume force, mass transfer-induced momentum source term, and porous media source term, respectively. Here, $\mu_{eff,q}$ is the effective viscosity of the corresponding phase, which includes the molecular viscosity $\mu_{m,q}$, the shear-induced turbulence viscosity $\mu_{t,q}$, and the bubble-induced turbulence additional viscosity μ_{BIT}. In this paper, the effect of bubble-induced turbulence is not considered, and the expression for $\mu_{eff,q}$ is as follows:

$$\mu_{eff,q}=\mu_{m,q}+\mu_{t,q} \tag{4}$$

Therefore, the Eulerian- Eulerian two-fluid model still needs to be closed with a turbulence model and an interfacial force model.

Chemical reactions affect the temperature of gas-liquid two-phase flow, and changes in temperature also act on changes in CO_2 solubility. The energy equation in the simulation can be expressed as:

$$\frac{\partial\left(\rho_l E\right)}{\partial t}+\nabla\cdot\left(u\left(\rho_l E+P\right)\right)=\nabla\cdot\left(k_{eff}\nabla T-\sum_i h_j\vec{J}_j\right)+S_h \tag{5}$$

where, E is the internal energy of the system, k_{eff} is the effective thermal conductivity, T is the temperature, h_j is the enthalpy of component j, $\vec{J}_j$ is the diffusion amount of component j and S_h is the chemical reaction source term.

2.2.2. Turbulence and interaction force model

The $k-\varepsilon$ model, proposed by Launder and Spalding [53], determines the length and time scales of turbulence by solving the transport equations for turbulent kinetic energy (k) and turbulent kinetic energy dissipation rate (ε). The standard $k-\varepsilon$ model has been widely applied in practical engineering flow calculations due to its stability, high computational efficiency, and strong applicability. Therefore, this paper adopts the standard $k-\varepsilon$ model for turbulence calculations, which can be expressed as [54]:

$$\frac{\partial\left(\rho_l k\right)}{\partial t}+\nabla\cdot\left(\rho_l k u_l\right)=\nabla\cdot\left(\left(\mu_{t,l}+\frac{\mu_{t,l}}{\sigma_k}\right)\nabla k\right)+G_k-\rho_l\varepsilon \tag{6}$$

$$\frac{\partial\left(\rho_l\varepsilon\right)}{\partial t}+\nabla\cdot\left(\rho_l\varepsilon u_l\right)=\nabla\cdot\left(\left(\mu_{t,l}+\frac{\mu_{t,l}}{\sigma_\varepsilon}\right)\nabla\varepsilon\right)+\frac{\varepsilon}{k}\left(C_{1\varepsilon}G_k-C_{2\varepsilon}\rho_l\varepsilon\right) \tag{7}$$

The liquid phase motion and turbulent kinetic energy generation rate can be calculated using the following formula:

$$\mu_{t,l}=C_\mu\rho_l\left(\frac{k^2}{\varepsilon}\right) \tag{8}$$

$$G_k=\mu_{t,l}\nabla u_l\cdot\left(\nabla u_l+\nabla u_l^T\right)-\frac{2}{3}\nabla\cdot u_l\left(3\mu_{t,l}\nabla\cdot u_l+\rho_l k\right) \tag{9}$$

In the equation, k is the turbulent kinetic energy, ε is the turbulent kinetic energy dissipation rate, $C_{1\varepsilon}$, $C_{2\varepsilon}$, C_μ, σ_k, and σ_ε are constants, and the values taken in this paper are: $C_{1\varepsilon}=1.44$, $C_{2\varepsilon}=1.92$, $C_\mu=0.09$, $\sigma_k=1.0$, $\sigma_\varepsilon=1.3$.

The most significant difference between two-phase flow and single-phase flow lies in the complex momentum exchange between the gas and liquid phases, which is typically modelled as various interfacial forces occurring at the gas-liquid interface. Examples of these forces include drag force F_D, lift force F_L, turbulent diffusion force F_{TD}, wall lubrication force F_{WL}, and virtual mass force F_{VM}. Interfacial forces are represented in the Eulerian two-fluid model as the source term F_{gL} in the momentum equation, with the physical meaning of the total momentum exchange between the two phases. The expression is as follows:

$$F_{gl}=F_D+F_l+F_{TD}+F_{WL}+F_{VM} \tag{10}$$

Some researchers have found that in a reactor with small bubbles, the direction of the lift force and the wall lubrication force are opposite, and the magnitudes of these forces are not significantly different [55, 56]. Meanwhile, Zhang et al. [57] conducted comparative studies on various interfacial force models, finding that virtual mass forces have little regulatory effect on bubble behaviour, while drag forces are considered the most important interfacial forces. Therefore, to reduce computational costs and improve computational efficiency, this study simulates only considers the effect of drag forces. The magnitude of drag forces is related to bubble size, slip velocity, and local gas content and it can be expressed as:

$$F_D=-\frac{3}{4}\alpha_g\rho_l\frac{C_D}{d_b}\left|u_l-u_g\right|\left(u_l-u_g\right) \tag{11}$$

In the equation, C_D is the drag coefficient, which is related to factors such as bubble size, shape, and two-phase properties. It is typically expressed as a relationship between the bubble Reynolds number Re_b and the Eotvos number Eo. These two dimensionless numbers are defined as follows:

$$Re_b = \frac{\rho_l |u_l - u_g| d_b}{\mu_l} \tag{12}$$

$$Eo = \frac{g d_b^2}{\sigma}(\rho_l - \rho_g) \tag{13}$$

where, d_b is the bubble diameter, g is the gravitational acceleration, and σ is the surface tension.

This paper adopts the empirical formula for drag coefficient proposed by Schiller-Naumann. The Schiller-Naumann model assumes that bubbles are spherical particles, and the drag coefficient under high and low bubble Reynolds numbers is determined by the following equation:

$$\begin{cases} C_D = \dfrac{24}{R_b}(1 + R_b^{0.687}) & R_b < 1000 \\ 0.44 & R_b \geq 1000 \end{cases} \tag{14}$$

2.3. Mass transfer in chemical reactions

2.3.1. *Species transport*

In the simulation, convection, diffusion, mixing, and chemical reactions of each component substance are represented by solving the species transport equation. The expression for the species transport equation is as follows:

$$\frac{\partial}{\partial t}(\alpha_q \rho_q Y_{q,j}) + \nabla \bullet (\alpha_q \rho_q u Y_{q,j}) = \nabla \bullet \left(\left(\rho_q D_{q,j} + \frac{\mu_l}{Sc_t} \right) \nabla Y_{q,j} \right) + S_j + R_j \tag{15}$$

where, $Y_{q,j}$ represents the mass fraction of the jth substance in the gas phase or liquid phase, $D_{q,j}$ is the diffusion coefficient of the substance, Sc_t is the turbulence Schmidt number, S_j is the mass source term, and R_j is the chemical reaction source term. The turbulence Schmidt number is defined as follows:

$$Sc_t = \frac{\mu_{eff,q}}{\rho_q D_t}, \tag{16}$$

Here, $\mu_{eff,q}$ is the effective turbulent viscosity in the turbulence model. D_t is the turbulent diffusion coefficient, which is taken as 0.7 in this paper.

CO_2 has low solubility in water, and the concentration of water is much higher than that of CO_2, so the reaction of CO_2 dissolving in water to form H_2CO_3 can be considered a pseudo-first-order reaction [58]. In a pseudo-first-order reaction, the chemical reaction rate is mainly determined by the concentration of CO_2. Meanwhile, only the inverse reaction of H_2CO_3 to produce CO_2 is considered in the simulation, without considering its further hydrolysis reaction. The final reaction equations are as follows:

$$CO_2 + H_2O \underset{k_{-1}}{\overset{k_1}{\rightleftharpoons}} H_2CO_3 \tag{17}$$

$$r_1 = k_1 [CO_2] \tag{18}$$

$$r_{-1} = k_{-1} [H_2CO_3] \tag{19}$$

where, r_1 and r_{-1} represent the forward reaction rate and reverse reaction rate, respectively, while $[CO_2]$ and $[H_2CO_3]$ denote molar concentrations. Similarly, k_1 and k_{-1} are the forward reaction rate constant and reverse reaction rate constant, respectively. It can be determined using the Arrhenius equation:

$$k_{1,-1} = Be^{-E_a/RT}, \tag{20}$$

Here B is the pre-exponential factor, E_a represents the activation energy, R represents the molar gas constant, and T is the absolute temperature. Their values are shown in the Table 2 [58]:

2.3.2. *Interphase mass transfer*

In present study, Henry's law was used to describe changes in CO_2 solubility. Henry's law states that at a constant temperature and under conditions where the total pressure is not too high. The liquid phase concentration at equilibrium in moderately or poorly soluble systems is directly proportional to the partial pressure of the gas phase. In this sense, the Henry constant is only a function of temperature and is independent of pressure:

$$c = P_g \cdot K_H, \tag{21}$$

where, c is the molar concentration of the gas dissolved in water, P_g is the partial pressure of the gas, and K_H is the Henry's constant.

Table 2. Activation energy and pre-factor.

Reactions	E_a (J/mol)	B
$CO_2 + H_2O \xrightarrow{k_1} H_2CO_3$	81.5×10^3	8.06×10^{12}
$H_2CO_3 \xrightarrow{k_{-1}} CO_2 + H_2O$	69.0×10^3	3.45×10^{13}

Table 3. PPI corresponding pore diameters.

PPI	Pore diameter (mm)
5	5.08
10	2.54
15	1.69
18	1.41
20	1.27
25	1.01
28	0.91
30	0.85
35	0.73
40	0.64
45	0.56
50	0.58

In this paper, the Vant's-Hoff equation is used to describe the change in Henry's constant at different temperatures:

$$K_H = K_{H0}\exp\left(-\frac{\Delta H_{soln}}{R}\left(\frac{1}{T}-\frac{1}{T_{ref}}\right)\right) \tag{22}$$

Among them, K_{H0} is the reference Henry coefficient, ΔH_{soln} is the dissolution enthalpy of CO_2, R is the gas constant, and T_{ref} is the reference temperature. In this paper, the values are as follows: $K_{H0} = 3.4\times10^{-4}\text{mol}\cdot\text{m}^3\cdot\text{Pa}^{-1}$, $\Delta H_{soln} = -19650\text{J/mol}$, $R = 8.314\text{J}\cdot\text{K}^{-1}\cdot\text{mol}^{-1}$, $T_{ref} = 298.15$ K.

Henry's law can determine the equilibrium ratio of CO_2 dissolution, and the corresponding gas-liquid mass transfer also needs to determine the liquid film mass transfer coefficient and the interface contact area. The mass transfer source term $\dot{m}_{gl}$ is defined as follows:

$$\dot{m}_{gl} = k_l A\left(K_q\rho_{g,m} - \rho_{l,m}\right) \tag{23}$$

where, K_q is the mass concentration equilibrium ratio, whose value is determined by Henry's law. $\rho_{g,m}$ and $\rho_{l,m}$ refer to the mass concentration in the gas phase and liquid phase, respectively. k_l is the liquid film mass transfer coefficient, and A is the phase interface contact area per unit volume. In this paper, an empirical model of liquid film mass transfer proposed by Brauer [59] is used, who argued that the liquid film mass transfer coefficient depends on the Schmidt number and the bubble Reynolds number (Re_b). Meanwhile, when calculating the contact area of the phase interface per unit volume, the bubble is assumed to be spherical. The calculations for k_l and A are as follows:

$$k_l = \frac{D_g}{d_b}\left(2 + 0.015Re_b^{0.5}Sc^{0.33}\right) \tag{24}$$

$$A = \frac{6\alpha_g}{d_b} \tag{25}$$

In the equation, D_g is the gas phase diffusion coefficient, and d_b is the bubble diameter.

2.4. Porous media model

In the simulation, the properties of the porous media are represented in the form of source terms in the momentum equation. The source term for porous media is defined as follows:

$$S_i = -\left(D_u\mu_q u_q + C_u\frac{1}{2}\rho_q|u_q|u_q\right) \tag{26}$$

where D_u is the viscous drag coefficient and C_u is the inertial drag coefficient, both of which are expressed as the characteristic parameters of porous media. They are related to the material of the porous media, porosity and pore size of the porous media. In this paper, the characteristic parameters of the ceramic porous media material can be determined by the following formula [60]:

$$D_u = \frac{1}{K_p} \tag{27}$$

$$C_u = \frac{3.5}{d_\varphi}\frac{1-\varphi}{\varphi^3} \tag{28}$$

where d_φ is the pore diameter and φ is the porosity. K_p is the permeability, defined as follows:

$$K_p = \frac{d_\varphi^{\,2}}{150}\frac{\varphi^3}{(1-\varphi)^2} \tag{29}$$

In this paper, pores per inch (PPI) is used to determine the pore diameter of porous diameter. Porous media parameters are shown in Table 3.

2.5. Boundary conditions

In order to reduce the computational cost and improve the computational efficiency, the following assumptions are made to simplify the simulation complexity based on the above control equations and mathematical models:

(1) Ceramic porous media materials are isotropic with uniform pore distribution and constant pore size. It is also considered that the density of carbon dioxide does not change in two-phase flow. Because the chemical reactions and dissolution processes are not violent, the changes in specific heat capacity, thermal conductivity, surface tension and diffusion coefficient of both are ignored.

(2) The temperature transfer is transient, ignoring the effects of thermal radiation and viscous dissipative heat. The chemical reaction is assumed to be a pseudo-first-order reaction. Also, because the temperature change is not significant, it can be assumed that the rate of the chemical reaction is only related to the concentration of carbon dioxide and not to the temperature.

(3) When modeling the interphase forces, only the influences of the two-phase drag forces are considered and the effects of the other two-phase forces are ignored. Meanwhile, the carbon dioxide bubbles are assumed to be spherical with a constant bubble diameter.

Based on the above assumptions, the boundary conditions in the simulation can be set correctly. The initial ambient temperature of the overflow carbonizer is 283.15 K. Meanwhile, the inlet temperatures of water and carbon dioxide are set to 275.15 K and 283.15 K, respectively. The inlet boundary condition is set to be a velocity inlet with a velocity magnitude determined by the experimentally measured volumetric flow rate. And the outlet boundary condition was selected as pressure outlet, which was set to be consistent with the experiment. According to the photos of CO_2 bubbles taken by the high-speed camera (will be shown in Fig. 3(b)), and taking into account the influence of the porous media, the bubble diameter was averaged and set to 0.06 mm. After several verifications in simulations and experiments, the volume fraction of initial CO_2 was set to be 0.5, which is more conducive to the iterative convergence and does not affect the steady state results. The boundary conditions in the simulation are as follows:

$$\begin{aligned} &T_{l,in} = 275.15K \quad , \quad T_{g,in} = T_{\infty} = 283.15K \\ &d_b = 0.06\text{mm} \quad , \quad \alpha_{g,initial} = 0.5283.15K \end{aligned} \tag{30}$$

$$u_{g,in} = \frac{Q_g}{A_{g,in}} \quad , \quad u_{l,in} = \frac{Q_l}{A_{l,in}}, \tag{31}$$

where T_{∞}, $T_{g,in}$ and $T_{l,in}$ are the ambient temperature, CO_2 inlet temperature and H_2O inlet temperature, respectively. Meanwhile, d_b is the bubble diameter, and $\alpha_{g,initial}$ is the initial CO_2 volume fraction. Meanwhile $u_{g,in}$ and $u_{l,in}$ represent the inlet velocities magnitude of CO_2 and H_2O. Q_g, Q_l, $A_{g,in}$, $A_{l,in}$ are CO_2 volume flow rate, H_2O volume flow rate, CO_2 inlet cross section area, and H_2O inlet cross section area, respectively.

2.6. Data reduction

The following parameters are defined in the performance evaluation of the overflow carbonizer. The velocity magnitude is defined as:

$$V = \sqrt{u_x^2 + u_y^2 + u_z^2} \tag{32}$$

where, V is the velocity magnitude, and u_x, u_y, and u_z are the velocity components in the x, y, and z directions, respectively.

The CO_2 absorption efficiency is then calculated using the CO_2 mass concentration in the liquid phase at the outlet, according to the following formula:

$$E_{absorption} = \frac{\rho_{co2,inlet}}{\rho_{co2,outlet}} \times 100\% \tag{33}$$

Here, $\rho_{co2,inlet}$ and $\rho_{co2,outlet}$ represent the mass concentration of CO_2 in the gas phase at inlet and the liquid phase at outlet, respectively.

When optimizing and designing overflow carbonizers, the relationship between CO_2 absorption rate and water pump energy consumption is a key consideration. The CO_2 absorption rate (A_{co_2}) and water pump energy consumption (W_{input}) are calculated using the following formulas respectively:

$$A_{co_2} = Q_g E_{absorption} \rho_g \tag{34}$$

$$W_{input} = Q_l \Delta P_l + \frac{Q_l \rho_l}{2}\left(V_{l,out}{}^2 - V_{l,in}{}^2\right) + Q_g \Delta P_g + \frac{Q_g \rho_g}{2}\left(V_{g,out}{}^2 - V_{g,in}{}^2\right) \tag{35}$$

In the equation, $V_{l,in}$ and $V_{g,in}$ are the inlet H_2O and CO_2 velocity magnitude. $V_{l,out}$ and $V_{g,out}$ are the outlet H_2O and CO_2 velocity magnitude. ΔP_l and ΔP_g is the liquid and gas pressure drop between the inlet and outlet.

3. Methods and Validation

3.1. Numerical methods

All numerical simulations were performed using the CFD commercial software FLUENT under double precision mode. The multiphase flow model (Eulerian-Eulerian two-fluid model) and the species transport model (finite-rate volumetric reaction) were opened for numerical simulation of interphase mass transfer and chemical reactions of CO_2 in the carbonizer. For the computational setup, the COUPLED method (coupled solution algorithm) is used to solve the control equations for pressure and velocity simultaneously. The PRESTO algorithm (pressure staggering option) is used for pressure discretization. The first-order upwind scheme was used to solve all equations and the transient time step was adjusted between 1×10^{-3} s and 3×10^{-3} s. In addition, the flow Courant number was set to 5 and the relaxation factors for pressure and momentum were set to 0.3 to ensure the accuracy and reliability of the simulations. The absolute convergence residual for all equations was set to 10^{-4}. During the simulation, the carbon dioxide concentration and pressure at the outlet of the overflow carbonizer are monitored as a function of time. When the monitored values remained constant or fluctuated regularly over time, the simulation was stopped, and subsequently, all flow and mass transfer characteristics were time-averaged.

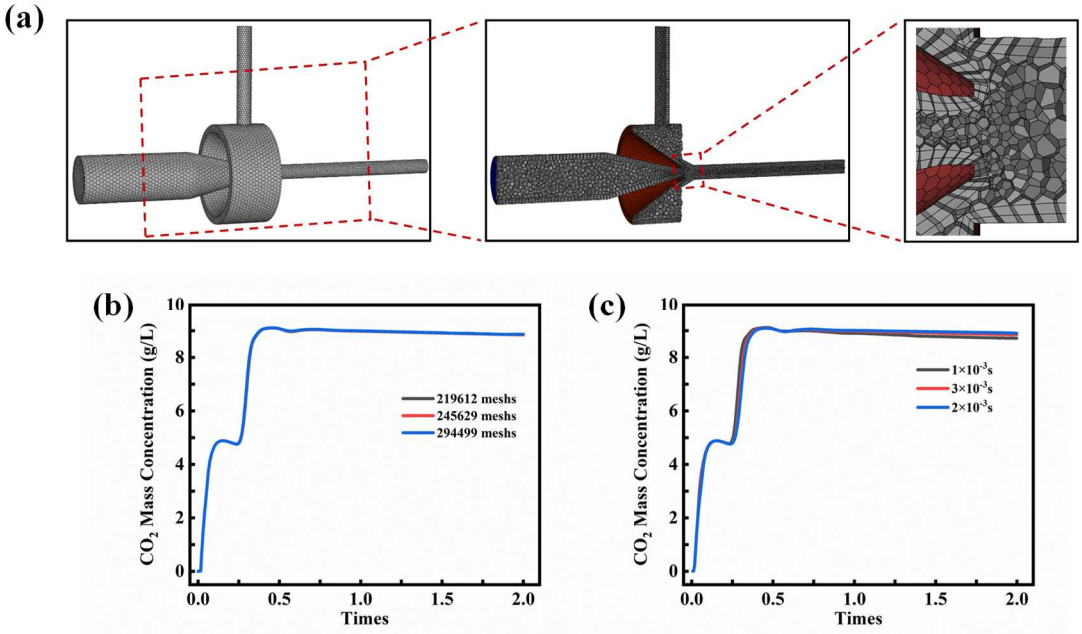

Fig. 2. (a) Local mesh schematic diagram, (b) Mesh independence verification, (c) Time independence verification.

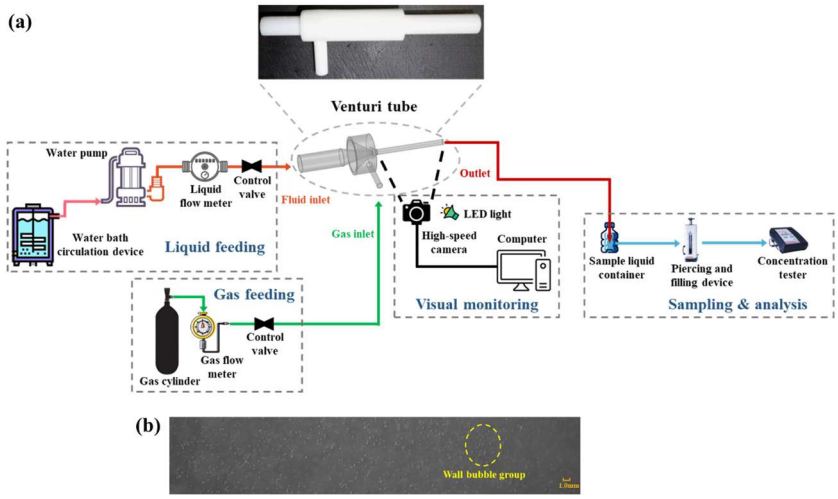

Fig. 3. (a) Flowchart of the experiment, (b) Image of CO_2 bubbles in the rear section.

3.2. Grid and time independence verification

This paper uses FLUENT Meshing to perform mesh generation on the overflow carbonizer model, selecting a polyhedral mesh type for high computational efficiency. To verify the calculation accuracy, a fully filled porous media carbonizer with $Q_g = 6L/\min$, $Q_l = 1.7L/\min$, $\varphi = 0.75$, and $PPI = 50$ is employed for mesh and time independence studies. A local mesh view of the overflow carbonizer model is shown in Fig. 2(a).

To ensure the accuracy of the results, grid independence and time independence were verified. As shown in Fig. 2, the analysis was performed for three mesh numbers (219612, 245629, 294499) and three time steps (1×10^{-3} s, 2×10^{-3} s, 3×10^{-3} s). Figures 2(b) and 2(c) demonstrate that the CO_2 outlet concentration variations over time show negligible discrepancies between different mesh numbers and time steps. Therefore, in order to ensure computational accuracy and efficiency, the simulations in this study were carried out using a mesh number of 245629 and a time step of 2×10^{-3} s.

3.3. Experimental validation

The flowchart of the experiment using H_2O solution for CO_2 absorption in a venturi tube is shown in Fig. 3(a), and this experiment was used to validate the numerical simulation results of CO_2 absorption. The experimental setup includes a venturi tube, a liquid feeding section, a gas feeding section, a visual monitoring section, and a sampling and analysis section. The liquid feeding section consists of a thermostatic water bath circulator, a high precision gear pump (Tuthill DGS1.2), a liquid flow meter (LZT M-15) and a control valve. Cryogenic water is drawn from the thermostatic water bath circulator via a gear pump, and the flow of water is regulated using a control valve and flow meter before being pumped into the liquid inlet of the venturi tube. In the gas feeding section, CO_2 flows from a small high-pressure cylinder and enters the gas inlet of the venturi tube after being regulated by a flow meter (LZM-4T) and a control valve. The high-velocity CO_2 and H_2O entering through the inlet undergo a violent exchange of momentum, mass, and heat in the venturi tube before exiting through the outlet. The experimental parameters are consistent with the simulation parameters in Section 4.1 of Table 4 (without porous media filling). For visual monitoring, a high-speed camera (PCO.dimax HS) and an LED illuminator (Multiled ST) were used to capture CO_2 bubbles and gas-liquid flow behavior in the rear section of the venturi. Figure 3(b) shows an image of CO_2 bubbles in the rear section of the venturi. As observed, the bubbles exhibit small and relatively uniform diameters, which supports the reasonableness of the assumptions in our numerical simulation.

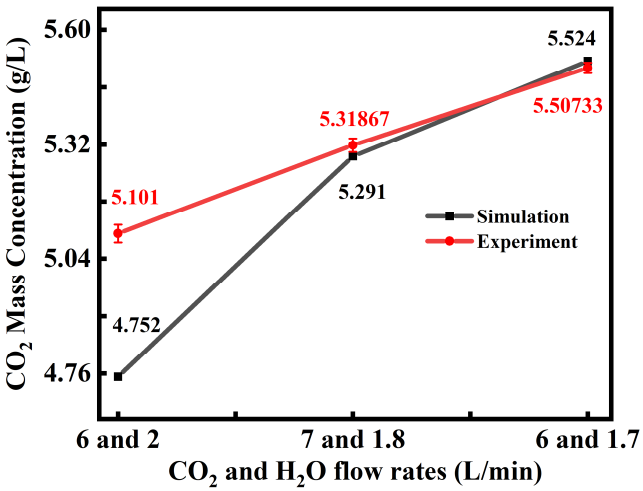

Fig. 4. Comparison of simulation and experimental results under different gas-liquid inlet flow rates.

In the sampling and analysis section, gas mixture samples were collected using a piercing sampling device (PFD standard), and the dissolved CO_2 concentration in water was measured with an Anton Paar CO_2 tester (CarboQC At-line). These experimental measurements will be validated against the CO_2 outlet concentration calculated from CFD simulations.

Figure 4 shows the curves of CO_2 outlet concentration (in the liquid phase) as a function of gas and liquid inlet flow rates, with data from both experimental measurements and simulations. In the experiments, each set of conditions was repeated at least three times. The average value was calculated only if the variation in the measured outlet CO_2 concentration did not exceed 0.1 g. From the figure, it can be seen that the simulation results are in good agreement with the experimental results under the working conditions of 7 and 1.8 L/min and 6 and 1.7 L/min for the gas-liquid inlet flow rates. At 6 and 2 L/min, the difference in CO_2 outlet concentration between the simulation and experimental results is 0.349 g/L, but the relative error is only 6.8%. The largest error originated from the instability of the gas-liquid two-phase flow, which manifested as fluctuations in the pump flow rate under high water flow conditions during the experiments. However, the simulated trend is consistent with the experimental results. The CO_2 outlet concentration in the liquid phase increases with gas and liquid inlet flow rates, indicating that the simulation model established in this paper is reliable.

4. Results and Discussion

First, the pressure loss and carbonization effect of the gas-liquid mixing device were compared under different inlet flow rates. Then, by analyzing the influence of changes in the local filling position of porous media, the optimal configuration for the local filling of porous media in the carbonizer tank is determined to meet the required carbon dioxide concentration in the bubble water. Finally, the effects of different pore size parameters were investigated for common porosities of porous media to reduce power consumption and enhance the mixing effect of carbon dioxide and water. In Section 4.1, the influence of three different flow rate conditions on gas-liquid mass transfer is analyzed under the complete filling of the porous media in the carbonizer tank. In Section 4.2, the influence patterns of four different configurations for locally filled porous media are discussed. Two common porosities (0.8, 0.9) are chosen for the parameter optimization in Section 4.3, and pore size parameters are chosen from 5-50 PPI (pores per inch). Detailed parameters for all cases are shown in Table 4.

4.1. Effect of different inlet flow rates

In this section, the dynamic effects of different inlet flow rates on the gas-liquid mixing process are systematically investigated. The gas-liquid mixing device studied is a completely filled porous media overflow carbonizer reactor with an integrated venturi structure. The porosity and pore size of the porous media are 0.8 and 50 PPI, respectively. Based on the experimental setup, three different combinations of gas-liquid inlet flow rates are discussed.

Figure 5 shows the comparative analysis of the system performance for different gas-liquid inlet flow rates at the intermediate cross section at 2 s. The velocity field distributions in Fig. 5(a) show that the distribution and change patterns are similar across different flow rates at the inlet, inside the pipe, and at the outlet. Due to the large gas flow rate and the coupled effect of the sudden narrowing of the pipe cross-section, a significant acceleration in velocity amplitude can be observed at the inlet and throat of the venturi tube. Inside the carbonizer tank, due to the flow-straightening effect of the porous media, the velocity amplitude is relatively stable in most areas, showing a more uniform low-velocity flow state. The velocity amplitude at the outlet section again shows a change with a small region of increased velocity, which may be due to the adjustment of the flow state caused by the smaller diameter of the pipe at the outlet.

Table 4. Detailed parameters of the gas-liquid mixing device.

Sections	CO_2 inlet		H_2O inlet		Outlet	Carbonizer tanks
	Q_{CO_2} (L/min)	T_{CO_2} (°C)	Q_{H_2O} (L/min)	T_{H_2O} (L/min)	Pressure (MPa)	Porous media filling method
4.1	6	10	2	2	0.103	Fully filled φ = 0.8, d_f = 50 PPI
	7	10	1.8	2	0.4	
	6	10	1.7	2	0.6	
4.2	7	10	1.8	2	0.4	Partially filled φ = 0.8, d_f = 50 PPI
4.3	7	10	1.8	2	0.4	Partially filled φ = 0.8, d_f = 5-25 PPI
	7	10	1.8	2	0.4	Partially filled φ = 0.9, d_f = 5-25 PPI

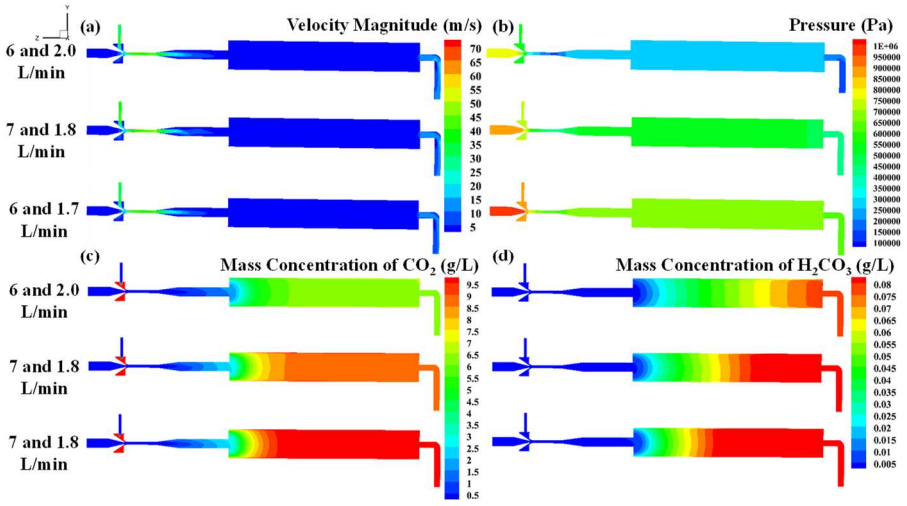

Fig. 5. Comparison of cases with different gas-liquid inlet flow rates at 2s: (a) velocity magnitude, (b) pressure distribution, (c) mass concentration of CO_2 in the liquid phase; (d) mass concentration of H_2CO_3.

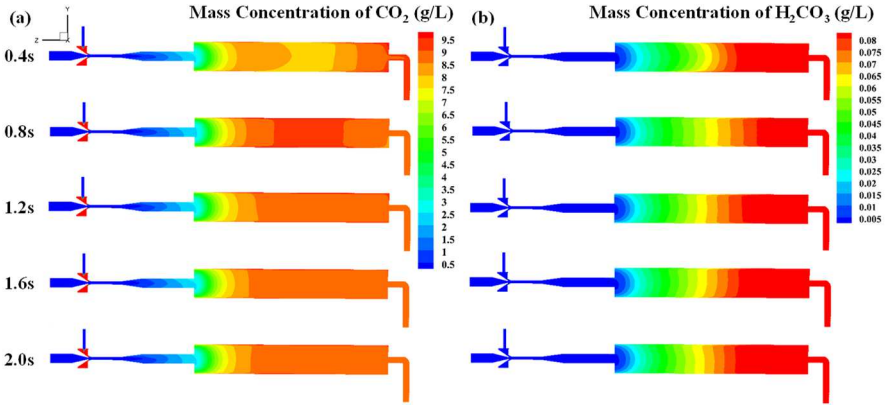

Fig. 6. Comparison of mass concentration of CO_2 and H_2CO_3 at different times: (a) mass concentration of CO_2 in the liquid phase, (b) mass concentration of H_2CO_3.

The pressure distribution shown in Fig. 5(b) indicates that the pressure values are relatively high at the inlet, especially at the H_2O end of the inlet. At the same time, as the inlet water flow rate decreases, the pressure also increases. This is because a lower water flow rate reduces the capacity to carry out CO_2, making it more likely to accumulate in the vacuum chamber. At gas-liquid flow rates of 6 and 2 L/min, the throat pressure drops dramatically to 550,000 Pa (approximately a 50% pressure drop), and the high water flow rate results in sharp pressure fluctuations, requiring reinforcement of the equipment structure to cope with mechanical stresses. The cushioning effect of the porous medium inside the carbonizer tank effectively dampens the oscillations, with pressure fluctuations attenuated and the pressure essentially the same as that at the end of the venturi. In the outlet section, the pressure value decreases slightly with the flow direction.

The distribution of liquid-phase carbon dioxide mass concentration shown in Fig. 5(c) indicates that, due to the vacuum chamber in the venturi tube, most of the CO_2 gas accumulates and fully develops in this area, resulting in a higher carbon dioxide mass concentration in this region. According to Henry's Law, at a constant temperature and under equilibrium conditions, the solubility of a gas in a liquid is directly proportional to the partial pressure of that gas. Therefore, a reduction in water flow weakens the water's flushing capacity, leading to the accumulation of carbon dioxide and an increase in gas partial pressure. This, in turn, enhances the solubility of CO_2 in water, resulting in an overall increase in the mass concentration of liquid-phase CO_2 within the carbonizer tank. Subsequently, the gas-liquid two-phase fluid flowing out from the venturi tube diffusion section enters the porous media carbonizer tank, and the CO_2 mass concentration gradually increases along the outlet. This indicates that in the porous media region, the CO_2 mass concentration significantly increases and becomes more uniformly distributed, and high-concentration carbonated water flows out from the outlet. In addition, apart from the influence of gas partial pressure, low flow input increases gas residence time and promotes efficient gas-liquid mixing. Combined with the high specific surface area of porous media, which increases the gas-liquid contact area, these factors further promote the increase in CO_2 concentration.

The mass concentration distribution of H_2CO_3 in Fig. 5(d) shows that the overall mass concentration of H_2CO_3 in the venturi tube is relatively low, and the concentration gradually increases along the outlet after entering the porous media carbonizer tank. H_2CO_3 exhibits different concentration levels at different flow rates, but the maximum concentration is only 0.08 g/L. This also indicates that the reaction of CO_2 dissolving in water is a reversible and relatively weak acid-base equilibrium process. Figures 5(c) and 5(d) display that the concentrations of carbon dioxide and carbonic acid exhibit consistent patterns of change. Both concentrations are significantly elevated and more uniformly distributed in the porous media carbonizer tank. It is worth noting that regions with higher CO_2 mass concentrations also have higher H_2CO_3 concentrations, indicating that the reaction of CO_2 dissolving in water to form carbonic acid occurs simultaneously.

Figure 6 illustrates the distribution of mass concentrations of CO_2 and H_2CO_3 in the liquid phase at several specific moments. Referring to the color scale on the right side of Fig. 6(a), at the initial moment (0.4s), the mass concentration of CO_2 changes gradually from approximately 3.5 g/L at the transition segment to a maximum of about 8.5 g/L at outlet, presenting an obvious axial concentration gradient. At 0.8s, the mass concentration distribution of CO_2 exhibits a more complex pattern, with high-concentration regions (7-8.5 g/L) interleaving with low-concentration regions (3-5 g/L). This is related to the dynamic evolution of

gas-liquid two-phase contact mass transfer and CO_2 dissolution processes, indicating that the mass transfer-reaction kinetic process is still in an unsteady state at this moment. At 1.6s and 2.0s, such inhomogeneity further intensifies and gradually stabilizes, and the high-concentration regions seem to show a tendency of aggregation or diffusion along the flow direction. In contrast, the mass concentration of H_2CO_3 is always within the range of 0.02-0.08 g/L, with similar distribution patterns at each moment. In terms of radial distribution, the concentration difference between the regions near the wall and the central area is small. Due to the slow reaction rate of CO_2 with water to form H_2CO_3 and the convective transport effect of fluid flow which transports the product toward the outlet, H_2CO_3 is enriched at the outlet. By comparing Fig. 6(a) and Fig. 6(b), it can be found that there is a certain correlation between the changing trends of CO_2 and H2CO3 mass concentrations at 0.8s. When the mass concentration of CO_2 shows obvious interleaved changes, the mass concentration of H_2CO also begins to rise rapidly and gradually reaches a stable state, which may imply a synchronous interaction mechanism between CO_2 and H_2CO_3.

Figure 7 presents a systematic performance evaluation of the overflow carbonizer under different gas-liquid inlet flow rates. The results reveal how local flow and pressure phenomena, induced by varying flow rates, determine the global carbonation efficiency through coupled hydrodynamic and mass transfer pathways. The transient water inlet pressure showed distinct behaviors: lower liquid flow rates (6 and 1.7 L/min) generated a higher peak pressure (1.1 MPa) and more pronounced fluctuations, whereas a higher liquid flow rate (6 and 2.0 L/min) led to rapid stabilization with a lower average pressure. This indicates that local pressure instability increases significantly as liquid flow decreases. These analyses can be used to optimize relevant processes or experimental conditions.

As practical applications require choosing the appropriate power pump based on the H_2O inlet pressure magnitude, Fig. 7(a) monitors the H_2O inlet pressure over time. When the reaction time is from 0-2.0s, there is a sharp rise at gas-liquid inlet flow rates of 6 and 1.7 L/min in the initial stage, reaching a peak value close to 1.1 MPa. Then it gradually declines and levels off, and the average pressure is maintained at 1 MPa. At flow rates of 7 and 1.8 L/min, the pressure also rises significantly but with a lower peak; it then levels off similarly, with the average pressure decreasing by approximately 15%. The rise at gas-liquid flow rates of 6 and 2.0 L/min is the smallest and reaches a steady state the fastest, with the average pressure dropping by about 20% compared with the case of 6 and 1.7 L/min. This indicates that both an increase in gas flow rate and a decrease in liquid flow rate will affect the inlet pressure at the water end, but the impact of liquid flow rate carries greater weight.

As shown in Fig. 7(b), at low inlet water flow rates, the total mass concentration of CO_2 and H_2CO_3 in the liquid phase rises more rapidly in the initial stage. At flow rates of 6 and 1.7 L/min, there is a significant initial rise followed by a fluctuating leveling off with a final mass concentration value of about 10 g/L. In contrast, when the flow rates are 7 and 1.8 L/min, the increase in gas flow rate causes more pronounced concentration changes, and the curve becomes volatile. Additionally, the increased water flow rate enhances the liquid's transport capacity, reduces the gas partial pressure, and shortens the gas residence time, resulting in a 10% decrease in the final total mass concentration. At flow rates of 6 and 2.0 L/min the rise is the most gentle and the final mass concentration value is the lowest, which is about 40% lower than the case of 6 and 1.7 L/min. In summary, the initial steep rise is attributed to the enhanced instantaneous mass-transfer driving force under high local pressure (via Henry's law), while the subsequent volatility stems from flow field destabilization. Conversely, the stable but low final concentration at high water flow rates is primarily limited by reduced gas residence time.

Figure 7(c) reveals that the average water inlet pressure and the average CO_2 and H_2CO_3 mass concentrations in the outlet liquid phase tend to increase linearly with decreasing H_2O inlet flow rate. High pressure favors the dissolution of gases and positive chemical reaction rates, promoting the formation and accumulation of CO_2 dissolved in water and H_2CO_3, thus increasing the mass concentration in the system. However, a critical transition occurs below water flow rates of 1.8 L/min: although pressure continues to rise, the rate of concentration increase diminishes. This inflection point indicates a regime of diminishing returns, where the global efficiency gain from higher pressure is offset by excessive flow instability and shortened effective contact time.

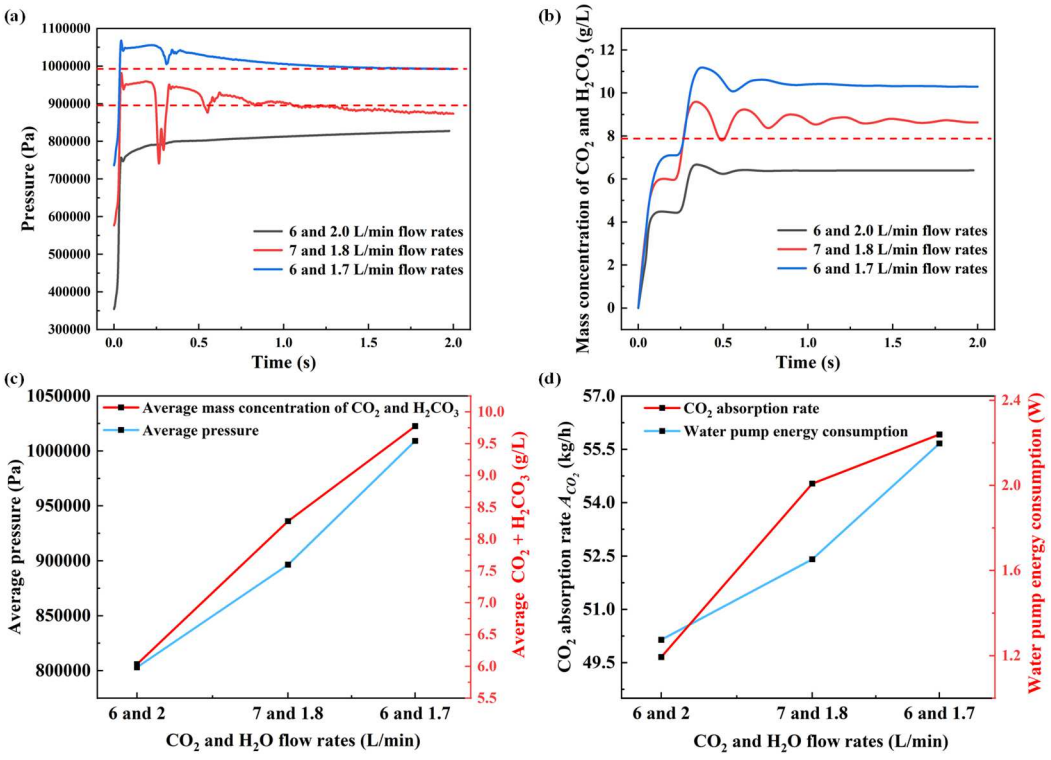

Fig. 7. Performance evaluation under different gas-liquid inlet flow rates: (a) H_2O inlet pressure versus time, (b) outlet mass concentration of CO_2 and H_2CO_3 in the liquid phase versus time, (c) time-averaged pressure and time-averaged mass concentration of CO_2 + H_2CO_3 in the liquid phase versus different inlet flow rates, (d) CO_2 absorption rate and Water pump energy consumption versus different inlet flow rates.

Furthermore, the relationship between CO_2 absorption performance and energy consumption was quantified in Fig. 7(d). Higher absorption rates required a disproportionate increase in water pump energy input. The non-linear scaling between absorption gain and energy penalty quantifies the trade-off inherent in the influence path from local conditions to global performance. Consequently, the gas-liquid flow rates of 7 and 1.8 L/min were identified as a balanced operating condition, offering a competitive carbonation efficiency without incurring the excessive energy penalty observed at more extreme conditions.

4.2. Effect of partial filling of porous media in carbonizer tanks

In this section, the effects of different partial filling configurations of porous media on mass transfer and energy consumption are systematically investigated. Based on the original overflow carbonizer, the porous media region is divided into four sections to study the influence patterns of different partial filling configurations. The selected gas-liquid flow rates are 7 and 1.8 L/min, with the porous media having a porosity of 0.8 and a pore size of 50 PPI.

Figure 8 shows the comparative analysis of the system performance at 2s for different filling modes at the intermediate section. The simulation results of the carbonizer tank at different porous media interval filling modes (1-3, 1-4, 2-3 and 2-4) show significant variations in pressure distribution, CO_2 and H_2CO_3 mass concentrations, in addition to velocity magnitude. These parameters are crucial for assessing energy efficiency and gas-liquid mixing performance.

Figures 8(a) and 8(b) show the velocity and pressure distributions for different filling modes. The venturi rapidly increases the flow velocity to 70 m/s at the throat due to the reduced cross-sectional area, which promotes intense turbulence and enhances mass transfer. Inside the carbonizer tank, the flow velocity is only 5-15 m/s, which is conducive to the full mixing of gas-liquid two-phase flow in the carbonizer tank. Due to the large difference in flow velocity between these two regions, the difference in flow velocity inside the carbonizer tank between different filling modes is not prominent. The overall pressure of 1-3 and 2-3 filling modes is reduced by about 0.02 MPa compared with the other modes. While the pressure gradient of 1-4 varies significantly, and the CO_2 inlet pressure of 1-4 and 2-4 filling modes reaches as high as 0.7 MPa at 2 s, which is a serious pressure hold-up implying a higher cost of energy consumption. Optimizing the filling structure to minimize pressure while ensuring adequate mixing is essential for energy-efficient operation.

To this end, Figs. 8(c) and 8(d) further discuss the effect of filling mode on the distribution of CO_2 and H_2CO_3 mass concentrations in the liquid phase. The plots of CO_2 and H_2CO_3 concentration distributions highlight the effect of the filler design on the uniformity of the reaction. The CO_2 mass concentration distributions show significant differences at different porous media spacing filling methods (1-3, 1-4, 2-3, 2-4). In the vacuum chamber area, carbon dioxide accumulates here, and the concentration of carbon dioxide in the liquid phase is usually high. With the fluid flow, the fluid at the inlet carries a high concentration of CO_2 and a certain amount of H_2CO_3 into the carbonizer tank. Different porous media spacer filling modes change the structure and porosity of the flow channel, thus affecting the gas dissolution and chemical reaction of the fluid. In the 1-3 and 1-4 filling modes, the low liquid phase fraction at the inlet of the carbonizer tank due to the porous media inhibits the dissolution of CO_2 and the reaction to form H_2CO_3. Thus, a region of low concentration is formed in the filling region near the inlet of the tank after entering from the inlet. However, the rate of CO_2 dissolution and chemical reaction increases rapidly in the second half of the process because the porous medium facilitates the fragmentation and mixing at the gas-liquid interface. In the 2-3 and 2-4 filling modes, there is a problem of insufficient dissolution of CO_2 in the high flow rate region at the inlet of the carbonizer tank and the reaction to produce H_2CO_3. However, the second half shows more uniform dispersion and an increase in H_2CO_3 concentration. It is worth noting that the increase in the mass concentration of H_2CO_3 is lower than that of CO_2.

To analyze more clearly the effect of different filling positions of porous media, Fig. 9 demonstrates the relationship between the area-averaged H_2O inlet pressure and the area-averaged outlet mass concentrations of CO_2 and H_2CO_3 in the liquid phase versus time as well as the filling position. As can be seen in Fig. 9(a), the pressure rises rapidly during the initial stage, followed by a gradual slowing down of the decreasing trend. This indicates that there is a rapid pressure release or depletion phase at the beginning of the reaction or process, and the system gradually stabilizes over time.

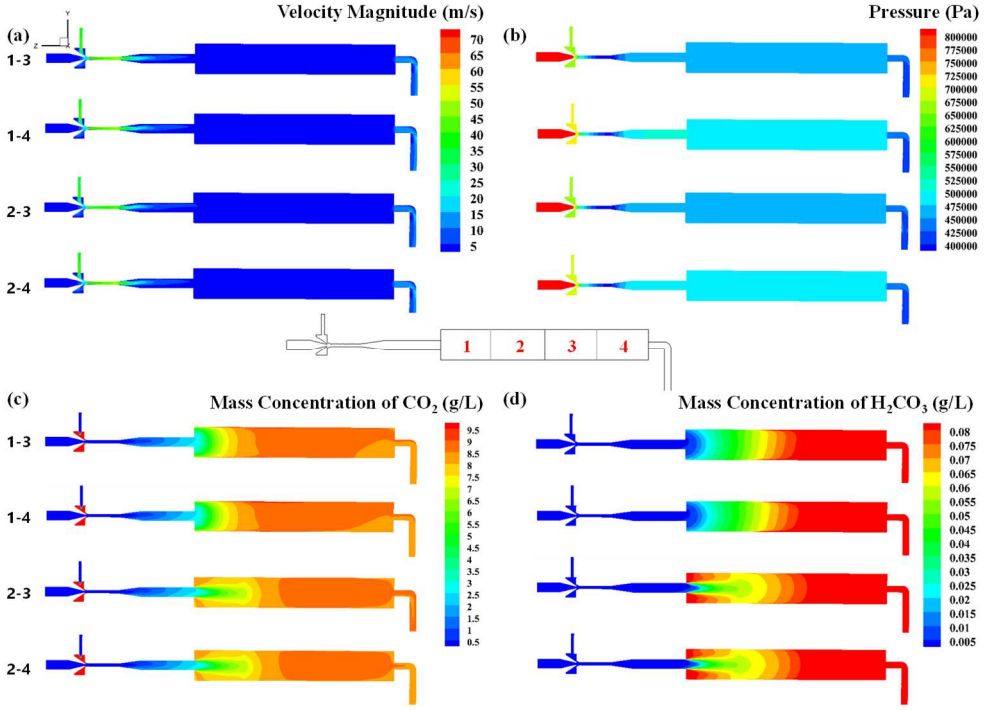

Fig. 8. Comparison of cases under different porous media spacer filling patterns in carbonizer tanks at 2s: (a) velocity magnitude, (b) pressure distribution, (c) mass concentration of CO_2 in the liquid phase, (d) mass concentration of H_2CO_3.

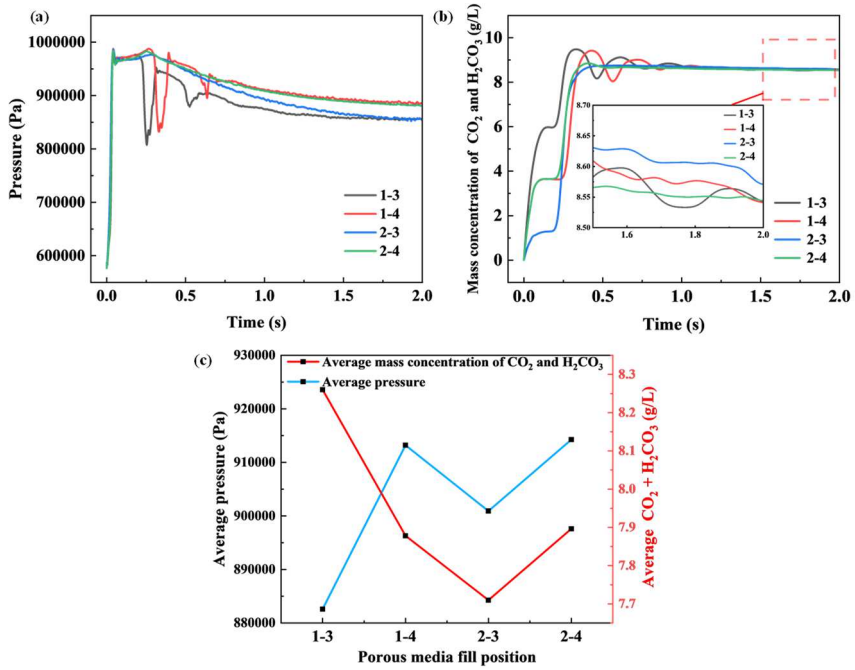

Fig. 9. Performance evaluation under different porous media spacer filling modes: (a) H_2O inlet pressure versus time, (b) outlet mass concentration of CO_2 and H_2CO_3 in the liquid phase versus time, (c) time-averaged pressure and time-averaged mass concentration of CO_2 + H_2CO_3 in the liquid phase versus different porous media spacer filling modes.

The overall trend of the pressure curves for different filling positions is similar, but there are some differences in the values, indicating that the filling position of the porous medium has a certain effect on the pressure change. In the initial stage (0-0.2 s), pressure pulses (0-0.9 MPa) occur in all filling methods. Among them, the 1-3 and 1-4 filling modes exhibit the steepest initial rise, indicating strong local flow confinement at the reactor inlet imposed by the porous media, which accelerates initial gas-liquid momentum transfer. In contrast, the 2-4 mode shows the lowest pressure peak (reduced by about 0.5%), suggesting that decentralized filling alleviates the initial hydrodynamic shock. In the mid-oscillatory phase (0.2-1.0 s), the 2-3 and 2-4 filling modes show small pressure fluctuations (±0.03 MPa) and the best stability. There are multiple pressure peaks for the 1-3 and 1-4 fillings. The 1-3 filling mode shows an oscillatory downward trend while the 1-4 fillings are generally higher than the other working conditions throughout the reaction process. During the steady state phase (> 1.0 s), the pressures at each position gradually approach each other as time increases. After about 1.6 s, the curves of 1-4 and 2-4, and 1-3 and 2-3 basically coincide, indicating that the effect of the filling position of the porous media on the pressure diminishes at the later stage. The 1-3 filling has a slightly lower pressure than the other filling modes, while symmetric shunt filling of 2-3 facilitates the homogenization of the pressure distribution.

As can be seen in Fig. 9(b), in the initial stage (0-0.5 s), the CO_2 and H_2CO_3 mass concentration in the liquid phase increases the fastest and has the highest peak value (about 9.5 g/L) in the 1-3 filling mode, followed by 1-4 filling mode. This is a direct consequence of the high local pressure and intensified turbulent mixing created by the inlet-positioned porous media, which enhances the initial CO_2 dissolution rate. Between about 0.2-0.6 s, the mass concentration profiles of all filling modes show relatively large fluctuations, suggesting that the generation or consumption of CO_2 and H_2CO_3 is not carried out steadily in the process and that there might be some periodic or intermittent reaction mechanisms. In the steady state phase (> 1.0 s), the mass concentrations of CO_2 and H_2CO_3 in the liquid phases of each condition are basically the same with the time. The filling of porous media 2-3 is slightly higher than in other cases, attributed to its more uniform pressure field that sustains stable mass transfer, but the difference is less than 0.1 g/L.

Figure 9(c) shows the time-averaged pressure and the time-averaged mass concentration of CO_2 and H_2CO_3 in the liquid phase versus the filling position of the porous media. A comprehensive evaluation of the pressure and mass concentration for each condition shows that the 1-3 filling method exhibits the best overall performance. In terms of pressure characteristics, the average operating pressure of this scheme is stable at 0.88 MPa, which is about 5% lower than the other cases. In terms of reaction efficiency, the average mass concentration of CO_2 and H_2CO_3 during the selected period reaches 8.3 g/L, which is an improvement of more than 5% compared with others. This advantage comes from the design of its porous media filling position, which ensures both flow stability and optimized reaction contact efficiency. It avoids the problem of excessive flow resistance in the inlet and outlet areas of the carbonizer tank for 1-4 and 2-4 filling and overcomes the defect of insufficient diffusion caused by untimely gas-liquid fragmentation and mixing in the 2-3 and 2-4 filling modes.

The time-averaged data in Fig. 9(c) quantifies the overall performance. The 1-3 configuration exhibits the optimal balance, with the lowest average pressure (0.88 MPa, about 5% lower) and the highest average concentration (8.3 g/L, > 5% higher). This superiority stems from a synergistic local-to-global influence path: the inlet-placed media creates a local high-pressure, high-turbulence zone that maximizes initial dissolution efficiency. Meanwhile, its specific spatial arrangement moderates overall flow resistance, preventing the formation of large-scale recirculation or dead zones that would degrade long-term, global carbonation efficiency. In contrast, the 2-4 mode's decentralized filling fails to create a sufficiently intense initial mixing zone, limiting early dissolution, while the 1-4 mode's configuration may induce excessive global flow resistance. Thus, the local deviation in flow structure dictates the global efficiency by controlling the trade-off between initial mass transfer enhancement and sustained, stable reaction contact.

4.3. Effect of porous media properties

This section further investigates the effect of porous media parameters on carbonizer efficiency and power consumption is further investigated. Based on the results analysis in Sections 4.1 and 4.2, a scheme with gas-liquid flow rates of 7 and 1.8 L/min and porous media filled in parts 1-3 was selected. The parameters of commercially available porous media are set for comparative performance analysis, respectively, with porosity of 0.8 and 0.9 and pore sizes of 5PPI, 10PPI, 15PPI, 20PPI, 25PPI and 50PPI.

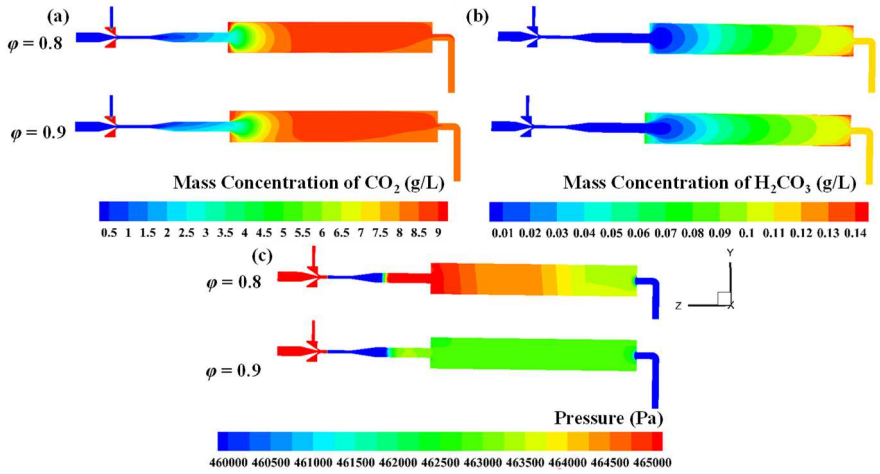

Fig. 10. Comparison of cases with different porosities (porous media filled in parts 1-3, 15PPI) in the carbonizer tank at 2 s: (a) mass concentration of CO_2 in the liquid phase, (b) mass concentration of H_2CO_3, (c) pressure distribution.

Figure 10 shows the distribution of CO_2 mass concentration in the liquid phase, H_2CO_3 mass concentration, and pressure when the carbonizer tank is filled with 15 PPI of porous media with different porosities (φ = 0.8, 0.9). Changes in porosity have a combined effect on the physicochemical processes in the carbonizer tank by influencing the diffusion of CO_2, the fluid flow characteristics, and the mass transfer processes of the reacting substances. It affects both the distribution of each physical quantity and the efficiency and homogeneity of the carbonizer reaction. The increase of porosity may make the contact between CO_2 and reactive substances more adequate, which is conducive to improving carbonizer reaction efficiency, but it may also change the tank's pressure environment, which needs to be considered in a comprehensive manner in order to optimize the carbonizer tank's design and operating conditions.

From the distribution of CO_2 mass concentration of the liquid phase in Fig. 10(a), it can be seen that it is consistent with the pattern observed in the previous section. Under these porous media parameters, because CO_2 easily accumulates in vacuum chamber, the CO_2 mass concentration in this area is also high. Then, A low concentration region exists locally in the filling area of the carbonizer tank front section impacted by the high fluid flow rate. However, due to the porous medium in this region promotes the gas-liquid interface of the broken and mixed, gas-liquid mixture in the fluid impact to the surrounding diffusion and flow with the fluid. As a result, the high concentration region is mainly distributed in the inlet and the second half of the carbonizer tank. After the second stage of porous media mixing, the CO_2 mass concentration further increased to about 9 g/L. At a lower porosity (φ = 0.8), the pores of the porous media are relatively small and complex, the diffusion paths of CO_2 molecules in them are tortuous and the diffusion resistance is larger. Therefore, the diffusion of carbon dioxide within the tank is relatively restricted, resulting in a wider region of lower mass concentration in the front section of the porous media carbonizer tank, with the mass concentration distribution exhibiting a more pronounced gradient change. In contrast, when the porosity is higher (φ = 0.9), the pore size and porosity are relatively larger, making carbon dioxide more susceptible to being flushed away by water flow. This results in the region with lower mass concentration at the front end of the porous media carbonizer tank becoming flatter, and the mass concentration changes becoming more gradual. This may also be related to the larger pore size, relatively higher flow velocity, and more vigorous flow, resulting in stronger convective transport of carbon dioxide, further leading to a more uniform mass concentration distribution.

From the distribution of H_2CO_3 mass concentration in Fig. 10(b), it can be seen that the production of H_2CO_3 is closely related to the concentration of CO_2 and its reaction conditions with other substances, but the overall production is low, only about 0.1 g/L. H_2CO_3 is mainly concentrated in the area of high CO_2 mass concentration and its vicinity, which leads to a certain correlation between the distribution of H_2CO_3 mass concentration and the distribution of CO_2 mass concentration, and the area of high concentration is relatively concentrated. Larger pores (φ = 0.9) favor mass transfer of the reacting substances, with more uniform diffusion of CO_2 and more adequate contact with the reacting substances. This promotes the carbonizer reaction, which affects the distribution of H_2CO_3 mass concentration.

The pressure distribution from Fig. 10(c) shows that, in porous media with a porosity of 0.8, due to the smaller and more complex pores, fluid flow through the carbonizer tank is subjected to a higher inertial resistance and the pressure inside the tank is relatively high. According to Darcy's law, a smaller porosity also leads to a larger pressure drop at the same flow rate. When the porosity increases to 0.9, the pores become larger and smoother, and the resistance to fluid flow decreases. But the above phenomenon also favors the dissolution of CO_2 in liquid and the enhancement of H_2CO_3 concentration. The smaller pressure drop at the same flow rate results in a lower overall pressure level in the tank and a corresponding smaller pressure gradient. As a result of the change in flow characteristics, the distribution of high and low pressure areas in the tank changes, and the pressure distribution is smoother.

Figure 11 systematically shows the variation of H_2O inlet pressure and CO_2 and H_2CO_3 outlet mass concentrations in the liquid phase with time during the reaction process for different PPI indices and porosities, as well as their relationship with the PPI index. Figures 11(a) and 11(b) mean H_2O inlet pressure versus time for both porosities show the same sharp rise in the initial stage up to a peak close to 1 MPa. Subsequently, it oscillates and decreases to an average pressure of 0.8 MPa-0.9 MPa. A comparison of the two porosity results reveals that pressure profiles at different PPI indexes show a more pronounced difference in porous media results for φ = 0.8 throughout the reaction process, while the effect is small at φ = 0.9.

During the initial period (0-0.5s), the porous medium with a pore size of 5 PPI shows a more rapid pressure rise, which may be attributed to its relatively loose and large pore structure. The reactants can diffuse and react quickly, and the fluid comes into contact with the large-area porous medium more quickly resulting in a sharp pressure rise. In contrast, the other PPI indices show a more moderate rise in working pressure, probably due to their relatively dense internal structure, longer diffusion paths of reactants and relatively fewer reaction sites. In the middle stage (0.5-1.2s), the pressure of each PPI index material reaches the peak and then starts to decline, but the rate and magnitude of the decline are different. The pressure of low PPI-index material decreased relatively fast, probably because its large pore structure made it easier for the fluid to diffuse or participate in the reaction. The relatively slow pressure drop in high PPI materials may be due to their relatively dense structure that hinders the diffusion of gases.

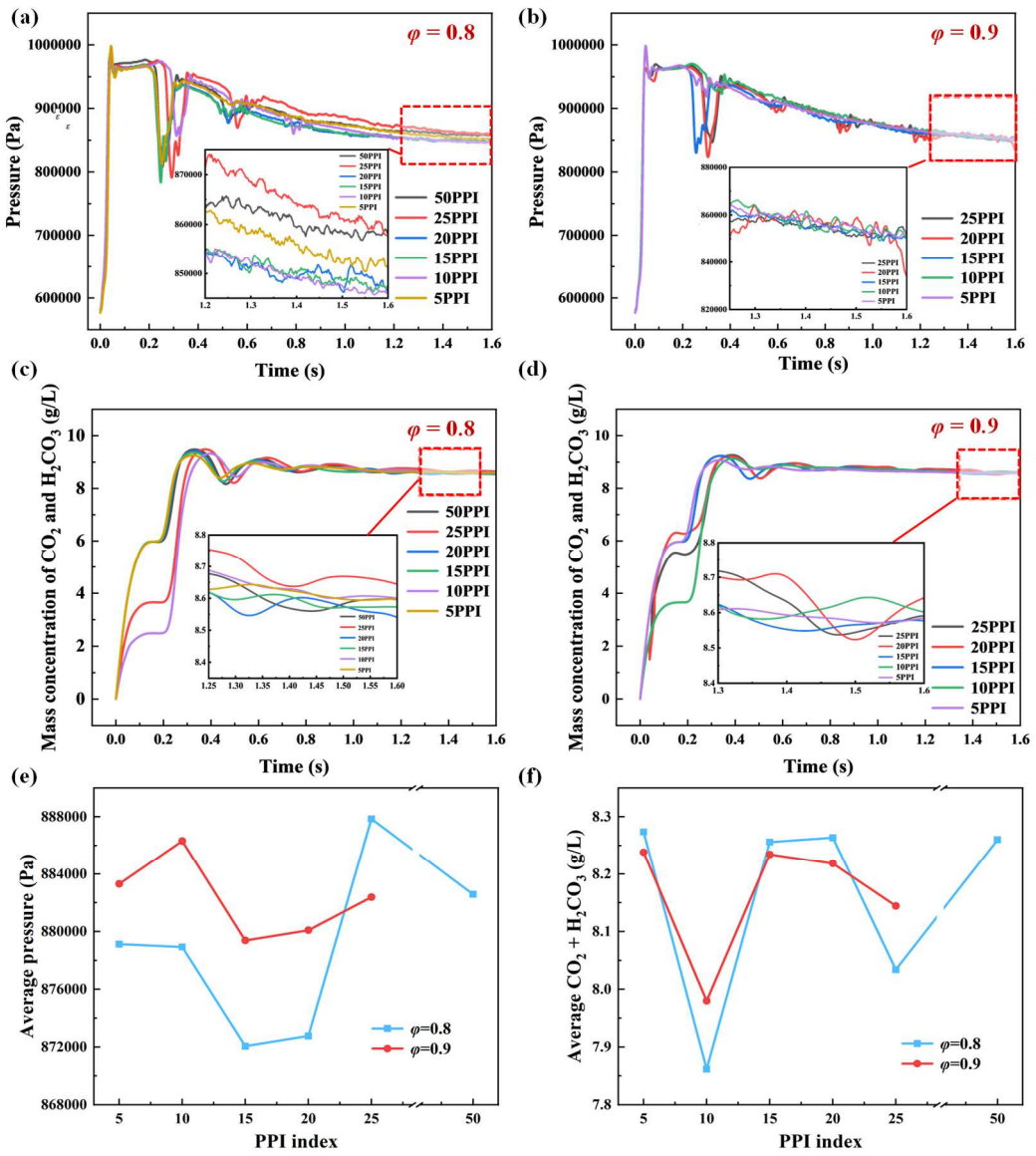

Fig. 11. Characterization of pressure and mass concentration variations at different PPI indexes and porosities: (a) H_2O inlet pressure versus time at φ = 0.8, (b) H_2O inlet pressure versus time at φ = 0.9, (c) outlet mass concentration of CO_2 and H_2CO_3 in the liquid phase versus time at φ = 0.8, (d) outlet mass concentration of CO_2 and H_2CO_3 in the liquid phase versus time at φ = 0.9; (e) time-averaged pressure versus PPI index; (f) time-averaged mass concentration of CO_2 and H_2CO_3 in the liquid phase versus PPI index.

In addition, the larger viscous resistance and inertial resistance coefficient also make the gas stay in the system for a relatively long time and the pressure drop is slower. In the later stage (after 1.2s), the pressure of each PPI index material tends to stabilize, indicating that the reaction reaches a dynamic equilibrium state. The average pressure of H_2O inlet is lower for cases filled with porous media with a pore size of 10-20 PPI.

Figures 11(c) and 11(d) show the total mass concentrations of CO_2 and H_2CO_3 in the liquid phase at the outlet as a function of time. The effect of PPI on the variation of CO_2 and H_2CO_3 mass concentration profiles varies nonlinearly with the increase of the porous media's PPI. In the initial phase (0-0.5s), the concentration profile with a pore size of 5 PPI rises fast but has the lowest peak value in the initial phase, while the pore size of 25 PPI is relatively slower but has the highest peak value. However, the difference in concentration between the two is only about 0.5 g/L. This may be because the structure of pore size 5PPI is more conducive to the diffusion of CO_2, which allows the highly concentrated solution to reach the outlet more quickly. However, the increased pore scale makes the mixing effect on the gas-liquid two-phase flow during the overflow carbonizer process, resulting in a higher peak concentration. It can be seen that both CO_2 diffusion efficiency and reaction efficiency together affect the variation of mass concentration, which is an important guidance for selecting appropriate PPI parameters for porous media. In the middle stage (0.5-1.2s), the mass concentration peaked at 0.55s and then started to decrease, but the time to peak and the value of the concentration varied among the porous media with different PPI indices. In the later stage (after 1.2s), the production and consumption of H_2CO_3 reached equilibrium. At φ = 0.8, the maximum difference in mass concentration at different PPI indices is about 0.2 g/L. At φ = 0.9, the effect of PPI is smaller and the maximum difference is only about 0.1 g/L.

To evaluate more clearly the effect of porous media parameters on the power consumption and carbonizer efficiency of the overflow carbonizer, the curves of the average H_2O inlet pressure and average mass concentration of CO_2 and H_2CO_3 in the liquid phase at the outlet versus the PPI index are evaluated in Figs. 11(e) and 11(f). The average H_2O inlet pressure in Fig. 11(e) directly reflects the fluid flow resistance; the higher the pressure, the higher the pumping energy consumption. Under low PPI index (5-15), the pressure decreases significantly, especially for porosity φ = 0.8, which has a large space for power consumption optimization. Under high PPI index (> 25), the pressure generally increases and the power consumption increases. For porosity φ = 0.8, the

pressure is lowest at PPI = 15 (about 0.872MPa), when the power consumption may be the smallest. While PPI = 20 is slightly larger, the difference between the two is small. This may be due to the low porosity media pore structure being more complex, and the local resistance to flow increases, but PPI = 15 and 20 due to structural matching to form a low-pressure region. When $\varphi = 0.9$, except for PPI = 25, the corresponding pressures of other pore sizes are higher than those at the overall porosity $\varphi = 0.8$. Moreover, the effect of pore size changes on pressure fluctuations is smoother, exhibiting lower pressure characteristics at high PPI values. This may be because high-porosity media have better pore connectivity and more uniform flow resistance, thereby avoiding local high-pressure energy dissipation points.

Figure 11(e) shows that in the PPI = 5-25 region, the outlet mass concentration of porosity $\varphi = 0.8$ fluctuates drastically from 7.8 to 8.3 g/L, and the adjustable range of concentration is larger. While the porosity $\varphi = 0.9$, the concentration varies from 8.0 to 8.25 g/L, which is relatively stable. At PPI > 25, the concentration peaked at both porosities (< 8.2 g/L), and the high PPI increased the cost of power consumption. When $\varphi = 0.8$, the mass concentration swings drastically with the change of the PPI index, and it plummets to 7.8 g/L at PPI = 10, with poor uniformity in the response. This may be due to the low porosity hindering mass transfer and local dead zones at specific pore sizes leading to inadequate reaction. At $\varphi = 0.9$, it shows an overall more uniform and stable carbonizer concentration, but the peak value is lower than that of low porosity. The high porosity improves the diffusion efficiency of CO_2, which promotes the dissolution of CO_2 in the liquid phase and the sufficient reaction with the liquid phase to form H_2CO_3. But it is also restricted by the limited reaction sites due to the reduction of specific surface area. After comprehensively evaluating the effects of power consumption and carbonizer concentration, the optimal porous media filling parameters are recommended to be porosity $\varphi = 0.8$ and PPI = 15-20. This combination maximizes the carbonizer concentration (> 8.2 g/L) and controls the pressure within a reasonable range (< 0.874 MPa), achieving the optimal balance between energy consumption and reaction efficiency.

5. Conclusion

This study investigates the energy loss and gas-liquid two-phase flow mixing performance in an overflow carbonizer integrating a venturi section and a porous-media-filled tank, focusing on the effects of gas-liquid inlet flow rates, porous media filling configurations, and pore structure parameters. It is recognized that the current work employs a simplified approach for bubble dynamics without incorporating a population balance model (PBM) and that the parametric scope and comparative benchmarks with standalone configurations are limited. These aspects will be addressed in future investigations. Through systematic numerical analysis validated against experimental data, optimal operational and structural parameters have been identified to achieve efficient carbonation while minimizing energy consumption. The main conclusions, which remain reliable for engineering application within the studied range, are as follows:

(1) Gas-liquid flow rates significantly influence gas-liquid mixing efficiency and system stability. Lower H_2O flow rates (e.g., 1.7 L/min) enhance CO_2 dissolution and H_2CO_3 formation but incur steep pressure drops and mechanical stresses. A balanced gas-liquid inlet flow rates of 7 and 1.8 L/min optimized carbonizer concentration (8-10 g/L) with manageable energy consumption, as further energy consumption increases yield diminishing returns due to reaction equilibrium limitations.

(2) Porous media filling modes critically affect flow dynamics and reaction uniformity. The 1-3 filling mode accelerates early-stage CO_2 dissolution, while symmetric filling (2-3) ensures steady-state uniformity. Compared to other configurations, 1-3 partial fill (front fill) achieves the best compromise between energy efficiency and carbonizer performance. The average pressure is reduced by 5% and the mass concentration of CO_2 and H_2CO_3 in the liquid phase is increased by 5%. This design mitigates flow resistance at the inlet while promoting gas-liquid interfacial fragmentation in the tank's rear section.

Porous media properties (porosity and pore size) govern mass transfer and power consumption. A porosity of 0.8 with 15-20 PPI pore size maximizes CO_2 dissolution (8.2 g/L) while maintaining low operational pressure (< 0.874 MPa). Lower porosity ($\varphi = 0.8$) exhibits higher pressure characteristics at high PPI values. Meanwhile, changes in pore size (caused by variations in PPI) have a more intense impact on pressure fluctuations. A higher porosity ($\varphi = 0.9$) enhances reaction uniformity, with a more gradual CO_2 mass concentration gradient distribution; however, at small PPI values (< 20), the pressure exceeds that of $\varphi = 0.8$ conditions.

The above research findings will provide insights for the further exploration of advanced porous media designs and multi-parameter optimization strategies for energy-efficient gas-liquid mixing systems in industrial carbonizer applications.

Author Contributions

Y. Gu and H. Pan developed the mathematical modeling, conducted the theoretical validation, and analyzed the empirical results; Y. Zhuang and Q. Luo undertook writing, review, editing, and supervision; designed the methodology; C. Ren performed the conceptualization, review and supervision. All authors discussed the results, reviewed the manuscript, and approved the final version.

Acknowledgments

The authors are very grateful for the reviewers' comments, and editors' recommendations through which the revision of the work has been improved with effective presentation of the research paper.

Conflict of Interest

The authors declare that there is no conflict of interest.

Funding

We would like to acknowledge the Grant support from the National Natural Science Foundation of China (52476063) and Midea Group's Technology Leadership Project (DWRKWHAX240700799).

Data Availability Statements

The datasets generated and/or analyzed during the current study are available from the corresponding author on reasonable request.

Nomenclature

A	Interfacial area per unit volume	$A_{g,in}$	Gas inlet cross-section area
$A_{l,in}$	Liquid inlet cross-section area	A_{co_2}	CO_2 absorption rate
B	Pre-exponential factor	c	Molar concentration of dissolved gas
C_D	Drag coefficient	C_u	inertial drag coefficient
C_μ	Constants in k-ε model	d_b	Bubble diameter
d_{pp}	Pore diameter	D_g	Gas phase diffusion coefficient
D_t	Turbulent diffusion coefficient	D_μ	Viscous drag coefficient
$D_{\alpha j}$	Diffusion coefficient of component j	E	Internal energy of the system
E_α	Activation energy	E_o	Eotvos number
F_D	Drag force	F_L	Lift force
F_{TD}	Turbulent diffusion force	F_{WL}	Wall lubrication force
F_{VM}	Virtual mass force	$F_{\sigma l}$	Total momentum exchange source term
g	Gravitational acceleration	h_j	Enthalpy of component j
J_j	Diffusion amount of component j	k	Turbulent kinetic energy
k_1	Forward reaction rate constant	k_{-1}	Reverse reaction rate constant
k_{eff}	Effective thermal conductivity	k_l	Liquid film mass transfer coefficient
K_H	Henry's constant	K_{H0}	Reference Henry coefficient
K_p	Permeability	K_q	Mass concentration equilibrium ratio
$\dot{m}_{gl}$	Mass transfer between phases	P_g	Partial pressure of gas
Q_g	Gas volume flow rate	Q_l	Liquid volume flow rate
r_1	Forward reaction rate	r_{-1}	Reverse reaction rate
R	Molar gas constant	R_j	Chemical reaction source term
Re_b	Bubble Reynolds number	S_h	Chemical reaction source term (Energy)
S_j	Mass source term	Sc_t	Turbulent Schmidt number
T	Temperature	T_∞	Ambient temperature
u	Velocity vector	u_{in}	Inlet velocity magnitude
V_{in}	Velocity magnitude at inlet	V_{out}	Velocity magnitude at outlet
W_{input}	Water pump energy consumption	$Y_{\alpha j}$	Mass fraction of component j

Greek symbols

α	Volume fraction	ε	Turbulent energy dissipation rate
μ_{eff}	Effective viscosity	μ_m	Molecular viscosity
μ_t	Shear-induced turbulence viscosity	μ_{BIT}	Bubble-induced turbulence viscosity
ρ	Density	ρ_m	Mass concentration
σ	Surface tension	σ_k	Constants in k-ε model
σ_ε	Constants in k-ε model	φ	Porosity

Subscripts

eff	Effectiveness	*g*	Gas phase
in	Inlet	*l*	Liquid phase
m	Mass / Molecular	*out*	Outlet
q	Phase indicator	*ref*	Reference value

References

[1] Lian, J.Z., Dimitrova, Y., Fasano, M., Sen, I., Cucurachi, S., Valorization of large-scale supply of carbonated water: A review, *Journal of Co2 Utilization*, 85, 2024, 102884.
[2] Lv, Z.Z., Du, H., Xu, S.J., Deng, T., Ruan, J.Q., Qin, C.L., Techno-economic analysis on CO2 mitigation by integrated carbon capture and methanation, *Applied Energy*, 355, 2024, 122242.
[3] Duggan Jr, J.E., Ogland-Hand, J.D., Middleton, R.S., Modeling, CCS policy support: Implications for market performance, net emissions, and welfare, *Applied Energy*, 389, 2025, 125613.
[4] Mahzari, P., Jones, A.P., Oelkers, E.H., An integrated evaluation of enhanced oil recovery and geochemical processes for carbonated water injection in carbonate rocks, *Journal of Petroleum Science and Engineering*, 181, 2019, 106188.
[5] Zhou, R.F., Ren, Y.X., Jiang, C.Q., Lu, Q.Y., Wastewater as a resource for carbon capture: A comprehensive overview and perspective, *Journal of Environmental Management*, 377, 2025, 124608.
[6] Solangi, N.H., Hussin, F., Anjum, A., Sabzoi, N., Mazari, S.A., Mubarak, N.M., Aroua, M.K., Siddiqui, M.T.H., Qureshi, S.S., A review of encapsulated ionic liquids for CO2 capture, *Journal of Molecular Liquids*, 374, 2023, 121266.
[7] Ono, Y., Tokuda, M., Sasayama, T., Kosaka, F., Matsuda, S., Kuramoto, K., Application of moving-bed reactor for effective hydrogenation of CO2

captured with a dual-function material to enhance the concentration of the gaseous product of methane, *Chemical Engineering Journal*, 505, 2025, 159585.
[8] Sheng, J., Wu, Y.S., Yu, Y.S., Zhang, Z.X., Wang, G.F., Numerical simulation of CO2 absorption process by mixture of MEA and single atom solution in hole jet reactor, *Fuel*, 396, 2025, 135334.
[9] Huang, R., Lin, M.Q., Tian, B.B., Xiao, C., A venturi reactor with an excellent mass transfer performance for carbon dioxide capture, *Journal of Environmental Management*, 360, 2024, 121144.
[10] Ding, G.D., Chen, J.Q., Lu, J.Q., Feng, Z.X., Ji, Y.P., Cai, X.L., Carbon dioxide stripping from acidic wastewater through a vortex venturi tubular microbubble generator, *Journal of Environmental Chemical Engineering*, 12(5), 2024, 113925.
[11] Fu, H.M., Xue, K.L., Li, Z.H., Zhang, H., Gao, D., Chen, H.P., Study on the performance of CO2 capture from flue gas with ceramic and PTFE membrane contactors, *Energy*, 263, 2023, 125677.
[12] Sumayli, A., Ahmed, Z., Jain, V., Roopashree, R., Kumar, A., Kashyap, A., Kumari, M., Gupta, S., Prasad, G.V.S., Abosaoda, M.K., Computational evaluation of micropores wetting effect on the removal process of CO2 through the membrane contactor, *Scientific Reports*, 15(1), 2025, 780.
[13] Chen, L., Ma, J.T., Chen, C., Wang, X., Qin, Y.H., Li, E.Z., Guo, Y.X., Peng, R., Pan, Z.H., How the dispersion and coalescence behaviors of CO2 bubbles affecting carbonation reaction in bubble column reactor: experimental and numerical simulation study, *Chemical Engineering Journal*, 512, 2025, 162675.
[14] Omidi, M., Baumann, T., Integrated numerical simulation of reactive bubble columns: A coupled approach with openFOAM and PhreeqC, *Chemical Engineering Journal*, 518, 2025, 163301.
[15] Han, H., Yan, J.S., Li, Y.X., Zhu, J.L., Wang, Y.F., Jing, R.D., Hu, Y.R., Simulating the reaction absorption of carbon dioxide by MEA aqueous solution in the RPB using three-dimensional Eulerian porous media approach, *Journal of Industrial and Engineering Chemistry*, 141, 2025, 610-625.
[16] Xu, H.Z., Yang, Z.Y., Li, Y.B., Cai, Y., Chen, A., Chu, G.W., Chen, J.F., Chemisorption of CO2 in a Liquid-Driven Rotating Packed Bed: A Mass Transfer Study, *Industrial & Engineering Chemistry Research*, 63(41), 2024, 17679-17690.
[17] Huang, J.K., Kang, S.F., Wan, M.X., Li, Y.G., Qu, X.X., Feng, F., Wang, J., Wang, W.L., Shen, G.M., Li, W., Numerical and experimental study on the performance of flat-plate photobioreactors with different inner structures for microalgae cultivation, *Journal of Applied Phycology*, 27(1), 2015, 49-58.
[18] Ulpts, J., Dreher, W., Klink, M., Thöming, J., NMR imaging of gas phase hydrogenation in a packed bed flow reactor, *Applied Catalysis a-General*, 502, 2015, 340-349.
[19] Plevan, M., Geissler, T., Abánades, A., Mehravaran, K., Rathnam, R.K., Rubbia, C., Salmieri, D., Stoppel, L., Stückrad, S., Wetzel, T., Thermal cracking of methane in a liquid metal bubble column reactor: Experiments and kinetic analysis, *International Journal of Hydrogen Energy*, 40(25), 2015, 8020-8033.
[20] Jin, N.D., Lu, H.W., Zhang, J.C., Ren, W.K., Characterization of Bubble Size of Gas-Liquid Two-Phase Flow Using Ultrasonic Signals, *IEEE Sensors Journal*, 24(10), 2024, 16867-16874.
[21] Zhai, L.S., Zhong, X.Y., Meng, X.Y., Pu, G.J., Jin, N.D., Mechanism of slug aeration in horizontal gas-liquid intermittent flow: Insights from S-PLIF and PIV analysis, *Chemical Engineering Journal*, 505, 2025, 159089.
[22] Ouyang, Y., Manzano, M.N., Wetzels, R., Chen, S.Y., Lang, X.J., Heynderickx, G.J., Van Geem, K.M., Liquid hydrodynamics in a gas-liquid vortex reactor, *Chemical Engineering Science*, 246, 2021, 116970.
[23] Chen, S., Lang, X., Kourou, A., Dutta, S., Van Geem, K.M., Ouyang, Y., Heynderickx, G.J., Enhancing CO2 capture efficiency: Computational fluid dynamics investigation of gas-liquid vortex reactor configurations for process intensification, *Chemical Engineering Journal*, 493, 2024, 152535.
[24] Bi, R.S., Tang, J., Wang, L.X., Yang, Q.Q., Zuo, M.L., Chen, C., Xiang, S.G., Experimental Study on Bubble Size Distribution in Gas-Liquid Reversed Jet Loop Reactor, *International Journal of Chemical Reactor Engineering*, 18(1), 2020, 20190102.
[25] Wen, T., Lu, L., He, W.F., Min, Y.R., Fundamentals and applications of CFD technology on analyzing falling film heat and mass exchangers: A comprehensive review, *Applied Energy*, 261, 2020, 114473.
[26] Lu, L.Q., Gao, X., Dietiker, J.F., Shahnam, M., Rogers, W.A., MFiX based multi-scale CFD simulations of biomass fast pyrolysis: A review, *Chemical Engineering Science*, 248, 2022, 117131.
[27] Kumari, R., Kasina, B., Gupta, R., Pant, H.J., Upadhyay, R.K., Effect of novel mixed impeller on local bubble size and flow regime transition in pilot scale gas-liquid stirred tank reactor, *Chemical Product and Process Modeling*, 19(2), 2024, 229-249.
[28] Teli, S.M., Mathpati, C.S., Experimental and Numerical Study of Gas-Liquid Flow in a Sectionalized External-Loop Airlift Reactor, *Chinese Journal of Chemical Engineering*, 32, 2021, 39-60.
[29] Chen, W.C., Fan, Y.W., Zhang, L.L., Sun, B.C., Luo, Y., Zou, H.K., Chu, G.W., Chen, J.F., Computational fluid dynamic simulation of gas-liquid flow in rotating packed bed: A review, *Chinese Journal of Chemical Engineering*, 41, 2022, 85-108.
[30] Chen, S.Y., Ouyang, Y., Vandewalle, L.A., Heynderickx, G.J., Van Geem, K.M., CFD analysis on hydrodynamics and residence time distribution in a gas-liquid vortex unit, *Chemical Engineering Journal*, 446, 2022, 136812.
[31] Lu, X., Xie, P., Ingham, D.B., Ma, L., Pourkashanian, M., Modelling of CO2 absorption in a rotating packed bed using an Eulerian porous media approach, *Chemical Engineering Science*, 199, 2019, 302-318.
[32] Shahsavari, N., Zhang, X.H., Microbubble-enhanced cold plasma activation for water decontamination: Degradation dynamics and energy yield in relation to pollutant concentration, total volume and flow rate of water, *Journal of Water Process Engineering*, 55, 2023, 104169.
[33] Lei, M., Guo, X., Yuan, S.H., Lu, S.B., Xu, X., Li, Q., Wang, Z.B., The self-circulating carbonation reaction based on Venturi-type bubble generator in the synthesis of pseudo-boehmite, *Fuel*, 381, 2025, 133387.
[34] Zhou, Y., Cui, J.Y., Chen, Z., Liu, J.C., He, L.P., Fan, W., Huo, M.X., Parametric analysis of venturi-type microbubble generator and the bubble fragmentation dynamics, *Desalination and Water Treatment*, 322, 2025, 101116.
[35] Liu, H.F., Li, C., Zhao, S.F., Zhu, H., Huang, Y.P., He, W., Zhao, Y., Li, Y.G., Guo, K., Design and structural parameter optimization of Venturi-type microbubble reactor for wastewater treatment by CFD simulation, *Journal of Flow Chemistry*, 14(1), 2024, 161-176.
[36] Zhou, L.T., Li, C.J., Chen, Y.K., Liu, H., Lin, M., Duan, J.H., Wang, W.W., Novel Venturi injector reactor design with multiple inlets in ammonia-nitrogen wastewater, *Separation and Purification Technology*, 363, 2025, 132062.
[37] Chen, Y.K., Zhang, X.X., Li, C.J., Zhou, L.T., Wang, W.W., Chen, G.H., Duan, J.H., Mass transfer enhancement and flow field simulations for a Venturi bubble generator with multiple inlet tubes, *Nuclear Engineering and Design*, 424, 2024, 113249.
[38] Ochoa, E.D., García, M.C., Padilla, N.D., Remolina, A.M., Design and experimental evaluation of a Venturi and Venturi-Vortex microbubble aeration system, *Heliyon*, 8(10), 2022, e10824.
[39] Pour, Y.D., Krasovitov, B., Fominykh, A., Hashemloo, Z., Kharaghani, A., Tsotsas, E., Levy, A., Intensification of spray drying granulation process by gas absorption accompanied by chemical dissociation reactions, *Chemical Engineering Journal*, 433, 2022, 133566.
[40] Yin, J., Zhang, J.R., Wang, C., Lv, N.X., Jiang, W., Liu, H., Li, H.P., Zhu, W.S., Li, H.M., Ji, H.B., Theoretical insights into CO2/N2 selectivity of the porous ionic liquids constructed by ion-dipole interactions, *Journal of Molecular Liquids*, 344, 2021, 117676.
[41] Li, H.X., Zhuang, Y.J., Feng, J.C., Huang, S.M., Experimental study on the solidification and melting performances of magnetic NEPCMs composited with optimized filling metal foam in a uniform magnetic field, *Solar Energy*, 263, 2023, 111927.
[42] Xu, W.B., Huang, Z.H., Zhuang, Y.J., Feng, J.C., Thermocapillary convection modes and phase change heat transfer characteristics of three-dimensional metal foam composited phase change materials with different aspect ratios under microgravity, *International Journal of Heat and Mass Transfer*, 222, 2024, 125155.
[43] Al-Jubouri, S.M., Al-Batty, S., Al-Hamd, R.K.S., Sims, R., Hakami, M.W., Haque, S.K.M., Sustainable environment through using porous materials: A review on wastewater treatment, *Asia-Pacific Journal of Chemical Engineering*, 18(4), 2023.
[44] Lamkhao, S., Tandorn, S., Rujijanagul, G., Randorn, C., A practical approach using a novel porous photocatalyst/hydrogel composite for wastewater treatment, *Materials Today Sustainability*, 23, 2023, 100482.
[45] Tang, Y.L., Luo, G., Cheng, Z.M., Packing size effects on the liquid circulation property in an external-loop packed bubble column, *AICHE Journal*, 68(12), 2022, e17851.
[46] Li, H., Zhang, Y., Yan, P., Li, X.G., Gao, X., Numerical analysis and experimental characterization of vortex flow at the gas-liquid interface in porous structure, *Chemical Engineering Research & Design*, 165, 2021, 445-455.
[47] Mao, J., Shi, W.B., Yi, O.Y., Zhang, X.Q., Zheng, B.D., Yang, H.J., Huang, Y.Y., Zhang, N., Ye, J., Xiao, M.T., Yang, Y.C., Modeling bubble dynamics in rotating foam stirrer reactors: A computational fluid dynamics approach incorporating gas-solid interactions, *AICHE Journal*, 71(8), 2025, e18874.
[48] Goel, P., Rabha, S.S., An Insight into the CO2 Adsorption and Temperature Evolution of a Zeolite Bed in a Fluidized Bed Reactor Using a Two-Fluid Modeling Approach, *Industrial & Engineering Chemistry Research*, 63(23), 2024, 10343-10352.
[49] Ali, H., Kim, K.W., Kwak, M.K., Kim, J.S., Choi, J.Y., Park, C.W., Numerical investigation on the flow mixing feature inside a continuously carbonating process tank, *Computers & Electrical Engineering*, 51, 2016, 343-355.

[50] Yao, Z., Yan, S., Wang, T., Chen, C., Xia, Z., Bubble breakup criteria for the population balance model of gas-liquid flow simulations, *Chemical Engineering Science*, 280, 2023, 119078.
[51] Launder, B.E., Spalding, D.B., *Lectures in Mathematical Models of Turbulence*, Academic Press, 1972.
[52] Xu, C., Liu, X., Gu, X., Computational studies of airlift and stirred airlift bioreactors with non-Newtonian fluid: A comparison of hydrodynamics and gas-liquid mass transfer, *Journal of Environmental Chemical Engineering*, 11(5), 2023, 110800.
[53] Tomiyama, A., Tamai, H., Zun, I., Hosokawa, S., Transverse migration of single bubbles in simple shear flows, *Chemical Engineering Science*, 57(11), 2002, 1849-1858.
[54] Cheung, S.C.P., Yeoh, G.H., Tu, J.Y., On the numerical study of isothermal vertical bubbly flow using two population balance approaches, *Chemical Engineering Science*, 62(17), 2007, 4659-4674.
[55] Zhang, X.-B., Yan, W.-C., Luo, Z.-H., CFD-PBM Simulation of Bubble Columns: Sensitivity Analysis of the Nondrag Forces, *Industrial & Engineering Chemistry Research*, 59(41), 2020, 18674-18682.
[56] Wang, X.G., Conway, W., Burns, R., McCann, N., Maeder, M., Comprehensive Study of the Hydration and Dehydration Reactions of Carbon Dioxide in Aqueous Solution, *Journal of Physical Chemistry A*, 114(4), 2010, 1734-1740.
[57] Brauer, H., Particle/fluid transport processes, *Progress in Chemical Engineering*, 19, 1981, 61-99.
[58] Jiang, P.X., Ren, Z.P., Numerical investigation of forced convection heat transfer in porous media using a thermal non-equilibrium model, *International Journal of Heat and Fluid Flow*, 22(1), 2001, 102-110.

ORCID iD

Yejie Gu https://orcid.org/0009-0005-6681-0457
Hongyu Pan https://orcid.org/0009-0008-7209-1788
Yijie Zhuang https://orcid.org/0000-0002-4318-4220
Quanquan Luo https://orcid.org/0000-0001-6857-5220

How to cite this article: Gu Y. et al., Numerical Study on Energy Loss and Gas-Liquid Two-Phase Mixing Characteristics in Overflow Carbonizer Reactor with Integrated Venturi-Porous Media Structure, *J. Appl. Comput. Mech.*, xx(x), 2026, 1–19. https://doi.org/10.22055/jacm.2026.48911.5593